Global Biogeochemical Cycles

RESEARCH ARTICLE
10.1029/2021GB007042

Radiocarbon in the Land and Ocean Components of the Community Earth System Model

Tobias Frischknecht[1,2], Altug Ekici[1,2], and Fortunat Joos[1,2]

[1]Climate and Environmental Physics, Physics Institute, University of Bern, Bern, Switzerland, [2]Oeschger Centre for Climate Change Research, University of Bern, Bern, Switzerland

Key Points:

- The uptake of bomb-produced ^{14}C by the ocean and land is simulated with the Parallel Ocean Model version 2 (POP2) and the Community Land Model, version 5.0 (CLM5)
- ^{14}C uptake by CLM5 is lower than observational estimates and carbon allocation and overturning in forest ecosystems are biased
- The deep ocean of POP2 is ventilated too slowly and radiocarbon ages are several centuries older than estimates from observations

Correspondence to:
F. Joos,
joos@climate.unibe.ch

Citation:
Frischknecht, T., Ekici, A., & Joos, F. (2022). Radiocarbon in the land and ocean components of the Community Earth System Model. *Global Biogeochemical Cycles*, *36*, e2021GB007042. https://doi.org/10.1029/2021GB007042

Received 16 APR 2021
Accepted 20 DEC 2021

Author Contributions:
Conceptualization: Fortunat Joos
Data curation: Tobias Frischknecht, Fortunat Joos
Formal analysis: Tobias Frischknecht
Funding acquisition: Fortunat Joos
Investigation: Tobias Frischknecht, Altug Ekici, Fortunat Joos
Methodology: Tobias Frischknecht, Altug Ekici, Fortunat Joos
Project Administration: Fortunat Joos
Supervision: Fortunat Joos
Visualization: Tobias Frischknecht
Writing – original draft: Fortunat Joos
Writing – review & editing: Tobias Frischknecht, Altug Ekici, Fortunat Joos

Abstract Large amounts of the carbon-isotope ^{14}C, entering Earth's carbon cycle, were produced in the atmosphere by atomic bomb tests in the 1950s and 1960s. Here, we forced the ocean and land components of the Community Earth System Model with atmospheric $^{14}CO_2$ over the historical period to constrain overturning time scales and fluxes. The uptake of bomb ^{14}C by the land model is lower than observation-based estimates. This mismatch is likely linked to too-low ^{14}C uptake by vegetation as the model overestimates $^{14}C/C$ ratios of modern soils. This suggests model biases in forest productivity or wood carbon allocation and turnover, and, in turn, a bias in the forest sink of anthropogenic carbon. The ocean model matches the observation-based global bomb ^{14}C inventories when applying the quadratic relationship between gas transfer piston velocity and wind speed of Wanninkhof (2014), https://doi.org/10.4319/lom.2014.12.351 and the wind products from Large and Yeager or the Japanese Reanalysis Project. Simulated natural radiocarbon ages in the deep ocean are many centuries older than data-based estimates, indicating too slow deep ocean ventilation. The sluggish circulation causes large biases in biogeochemical tracers and implies a delayed deep ocean uptake of heat and carbon in global warming projections. Our study suggests that ^{14}C observations are key to constrain carbon fluxes and transport timescales for improved representations of land and ocean biogeochemical cycles and Earth system model projections.

1. Introduction

Radiocarbon (^{14}C) is produced naturally in the upper atmosphere by cosmic rays (Masarik & Beer, 2009). In addition, large amounts of ^{14}C were injected into the stratosphere as a byproduct of nuclear bomb tests in the 1950s and 1960s (Enting, 1982). Natural and bomb-produced ^{14}C is quickly oxidized to $^{14}CO_2$ and becomes part of the Earth's carbon cycle (Siegenthaler, 1989). ^{14}C, unlike the stable ^{12}C and ^{13}C isotopes, decays radioactively with a mean half-life of 5,700 years (Bé et al., 2013). The decay rate serves as a clock once carbon is isolated from the atmosphere. Radioactive decay is too slow to have noticeably affected bomb ^{14}C up to now and bomb ^{14}C is, similar to anthropogenic CO_2, conserved and redistributed among atmosphere, ocean, and land biosphere. On the other hand, carbon in the deep ocean and soils is depleted in natural ^{14}C with respect to atmospheric carbon because of radioactive decay (Oeschger et al., 1975; Revelle & Suess, 1957). The slower the carbon exchange with the atmosphere the larger the depletion. Observations of the transient, pulse-like bomb ^{14}C signal and the natural $^{14}C/C$ ratio provide therefore constraints on the uncertain time scales of exchange of carbon and other tracers between and within different Earth system components. These constraints are important as correctly representing the overturning time scales (Bolin & Rodhe, 1973) and exchange fluxes of carbon, heat, and other tracers is a prerequisite to reliably model biogeochemical cycles and project the fate of anthropogenic CO_2 and global warming.

The specific goal of this study is to evaluate the representation of carbon fluxes and transport time scales in the ocean and land components of the Community Earth System Model (CESM) with ^{14}C observations. The Earth system budget of bomb ^{14}C is established by comparing bomb ^{14}C production statistics and inventory changes in the atmosphere, ocean, and land biosphere. The purpose is to identify model biases in transport timescales and fluxes to stimulate further model development for improved representations of tracer transport and Earth system projections.

The ^{14}C variations of the recent past and the modern distribution of ^{14}C in the Earth system are documented by compilations from various climate archives such as tree rings and corals (Dentith et al., 2019; Druffel, 2002; Grottoli & Eakin, 2007; Reimer et al., 2020), and modern sampling in the atmosphere, ocean, and land biosphere (Lawrence et al., 2020; He et al., 2016; Key et al., 2004; Levin et al., 2010; Shi et al., 2020; Turnbull et al., 2017).

Atmospheric $^{14}C/C$ varied relatively little over the past few millennia before the first nuclear bombs detonated (Hogg et al., 2020; Reimer et al., 2020). The tropospheric $^{14}C/C$ ratio almost doubled within a decade before a nuclear test ban treaty was set in place in 1963 (Naegler & Levin, 2009a). Thereafter, tropospheric$^{14}C/C$ ratio and the ^{14}C inventory of the atmosphere declined due to continued bomb ^{14}C uptake by the ocean and land biosphere (Broecker et al., 1985; Lawrence et al., 2020; He et al., 2016; Hesshaimer et al., 1994; Joos, 1994). The emissions of ^{14}C-free fossil CO_2 forced an additional negative trend in atmospheric $^{14}C/C$ (Graven, 2015; Naegler & Levin, 2006; Suess, 1955). Small anthropogenic ^{14}C sources stem from the nuclear power industry (Graven & Gruber, 2011; Zazzeri et al., 2018). For convenience, the terms "bomb" and "excess" are used interchangeably in this manuscript to describe the changes in $^{14}C/C$ and ^{14}C inventories due to all processes, including natural variability, since 1945.

Measurements documenting bomb ^{14}C in vegetation and soils are relatively scarce and do not permit to directly establish the bomb ^{14}C inventory of the global land biosphere. Naegler and Levin (2009a) estimated the bomb ^{14}C evolution in the land biosphere by the difference between total ^{14}C production estimated from bomb-test statistics, the observed change in the atmospheric inventory and the observation-constrained uptake by the ocean. Naegler and Levin (2009b) used their bomb inventory reconstruction in combination with a three-box land biosphere model to estimate global net primary productivity (NPP) to 41–64 GtC yr^{-1}. The representation of NPP and carbon turnover time scales is essential to simulate the terrestrial sink of anthropogenic carbon (Thompson et al., 1996). The global observational constraint of Naegler and Levin (2009a) has, however, not yet been applied by others to evaluate NPP and carbon allocation and turnover of spatially resolved state-of-the-art terrestrial models.

For comparison with observations and improved process understanding, ^{14}C has been implemented in box models (Broecker et al., 1985; Naegler & Levin, 2006; Oeschger et al., 1975; Siegenthaler & Joos, 1992), dynamic ocean circulation models (Jahn et al., 2015; Matsumoto et al., 2004; Mouchet, 2013; Rodgers et al., 2004; Toggweiler et al., 1989), spatially resolved land biosphere models (Koven et al., 2013; Randerson et al., 2002; Roth & Joos, 2013), and atmospheric transport (Braziunas et al., 1995; Krakauer et al., 2006; Randerson et al., 2002; Rodgers et al., 2011) and transport-chemical models (Kanu et al., 2016). The ocean modeling community and the Coupled Climate-Carbon Cycle Model Intercomparison Project established protocols to simulate the uptake and distribution of natural and bomb ^{14}C (Jones et al., 2016; Orr et al., 1999, 2017) for the evaluation of transport time scales and water mass age (Khatiwala et al., 2012).

While many studies are addressing ^{14}C in dynamic ocean models, ^{14}C simulations with spatially resolved land biosphere models are scarce and simulations with state-of-the-art Earth System Models addressing the budget of bomb ^{14}C and air-sea and air-land fluxes are missing. Thus far, the models participating in the Coupled Model Intercomparison Project (Eyring et al., 2016), which are used for carbon cycle and climate projections in the assessments of the Intergovernmental Panel on Climate Change, have generally not been evaluated against ^{14}C observations. This offers the opportunity to confront these models with the rich set of ^{14}C observations toward improving the representation of tracer transport timescales and biogeochemical cycles and projections of heat and carbon uptake by ocean and land, ocean acidification and deoxygenation, sea-level rise, and global warming.

Recently, carbon isotopes were added to the marine (Jahn et al., 2015) and land biosphere components (Keller et al., 2017; Koven et al., 2013; Oleson et al., 2013) of the CESM. Shi et al. (2020) compared $\Delta^{14}C$ of soil carbon as simulated with the Community Land Model, version 5 (CLM5) with their soil $\Delta^{14}C$ data and document younger soil ages in the CLM5 than measured. Jahn et al. (2015) applied the Parallel Ocean Model version 2 (POP2) with 3° horizontal resolution and find the oceanic ^{14}C bomb uptake to be reasonably well simulated compared to observations. Here, we build on this earlier work and present results from ^{14}C-enabled simulations with the standard version of POP2 with a nominal horizontal resolution of 1° and with CLM5 for the preindustrial state and the historical period. POP2 (Danabasoglu et al., 2012, 2020) and CLM5 (Lawrence et al., 2019; Kennedy et al., 2019; Lombardozzi et al., 2020) are standard components of CESM version 2 (Danabasoglu et al., 2020; Hurrell et al., 2013) and are used here in a so-called stand-alone mode driven by atmospheric forcing data. POP2 simulations over the historical period are performed with two wind products, the Large and Yeager Normal Year Forcing (NYF, Large and Yeager (2009)) and the Japanese Reanalysis project (JRA-55, Kobayashi et al. (2015)) data, to investigate the sensitivity of results to the wind forcing and to evaluate the piston velocity parameterization for specific wind products against observational bomb ^{14}C data.

We analyze the bomb ^{14}C budgets of the Earth, the ocean, and the land biosphere to evaluate the land and ocean components of CESM2. The modeled evolution of the bomb ^{14}C inventory of the land biosphere is compared with the observational estimate of Naegler and Levin (2009a). We further compare estimates of the global ocean bomb ^{14}C inventory established from marine measurements, the temporal evolution of surface ocean $^{14}C/C$ during the bomb period as recorded by corals and bivalves, and the gridded bomb $^{14}C/C$ data from the Global Ocean Data Analysis Project (GLODAP) with model results. The observed changes in the atmospheric bomb ^{14}C inventory and the bomb ^{14}C production record allow us to estimate whether the combined bomb ^{14}C uptake by the ocean and the land biosphere models is simulated in agreement with observations. Finally, we compare modeled and measured $^{14}C/C$ in the deep ocean to assess the model's ventilation time scales and discuss related model-data biases for biogeochemical tracers. Next, we describe briefly POP2, CLM5, and the model setup; readers not interested in these sections may directly continue with Section 2.4.

2. Methods

2.1. Ocean Model: POP2/MARBL

POP2 is run on the standard model grid with 60 vertical layers and a horizontal resolution of about 1° and finer resolution around the equator. The marine biogeochemical cycle is based on the Biogeochemical Elemental Cycling (BEC) model (Moore et al., 2002, 2004) and handled by the Marine Biogeochemistry Library (MARBL). It represents the cycling of carbon, the carbon isotopes ^{13}C and ^{14}C, nitrogen, phosphorus, iron, silica, oxygen, and alkalinity. Carbon isotopes are exchanged between the seven tracers: dissolved inorganic carbon (DIC), dissolved organic carbon (DOC), calcium carbonate ($CaCO_3$), and three different phytoplankton (small phytoplankton, diatoms, and diazotrophs) and one zooplankton pool.

The net air-to-sea gas flux of CO_2, $F_{a,s,\mathrm{net}}$, is modeled as the product of the piston velocity and the difference between the saturation, C_{sat}, and surface water, C_s, concentration of dissolved CO_2 following Wanninkhof (2014):

$$F_{a,s,\mathrm{net}} = (1 - a_{\mathrm{ice}}) \cdot a \cdot u_{10}^2 \cdot \left(\frac{660}{\mathrm{Sc}_{\mathrm{CO}_2}}\right)^{0.5} \cdot (C_{\mathrm{sat}} - C_s) = k \cdot (C_{\mathrm{sat}} - C_s) \quad (1)$$

a_{ice} is the fraction of a grid cell covered by ice, a is a scaling factor, u_{10} is the wind speed at 10 m above sea level, and $\mathrm{Sc}_{\mathrm{CO}_2}$ the Schmidt number of CO_2, and k the piston velocity with respect to the liquid phase. A similar approach is used for computing the air-to-sea gas fluxes of the isotopes of CO_2. The scaling factor a is set to 0.251 cm hr^{-1}/(m s^{-1})^2 as in Wanninkhof (2014), substantially lower than the value of 0.31 cm hr^{-1}/(m s^{-1})^2 assumed by Jahn et al. (2015). This downward revision of the piston velocity is broadly in agreement with earlier re-assessment of the bomb-produced radiocarbon distribution within the ocean (Müller et al., 2008; Peacock, 2004; Sweeney et al., 2007). The value of a is tied to the applied wind product and its use with other wind products may lead to different air-sea fluxes and, in turn, bomb ^{14}C inventory and $\Delta^{14}C$ values. The global mean piston velocity normalized to a Schmidt number of 660 is 15.7 cm hr^{-1} for NYF and 17.0 cm hr^{-1} for the JRA-55 product evaluated over the entire ocean, including ice-covered areas. These values are within the lower range of the estimate by Naegler (2009). Wind speeds and piston velocities from NYF are, compared to JRA-55, much lower over ice-covered regions and generally higher in mid-latitude areas and the northern North Atlantic (Figure A1).

^{14}C is, as ^{13}C and carbon, cycled between all carbon pools. Fractionation of ^{13}C versus ^{12}C is implemented, as described by Jahn et al. (2015), following Zhang et al. (1995) for air-sea gas exchange and following Laws et al. (1995) for photosynthesis. Fractionation for ^{14}C is twice as large as for ^{13}C. Besides, a so-called "abiotic" ^{14}C tracer is implemented in POP2 (Jahn et al., 2015). Abiotic ^{14}C does not cycle through the organic matter pools and the fractionation factors for air-sea gas exchange fluxes are set to unity. The abiotic implementation is a simplification, but requires much less computing resources than the biotic implementation. ^{14}C decays in POP2 with a half-life of 5,730 years. We note that the value of the half-life has recently been updated based on new measurements to 5,700 years (Bé et al., 2013; Orr et al., 2017) but this small revision has not yet been implemented in CESM. The standard ratios for $^{13}C/^{12}C$ and $^{14}C/C$ are set to unity in the POP2 model. Model units are converted by applying the standard $^{14}C/C$ ratio of $1.176 \cdot 10^{-12}$ for the computation of ^{14}C inventories.

2.2. Land Model: CLM5.0

CLM5.0 represents terrestrial carbon and nitrogen dynamics and features various vegetation, litter, and soil organic matter pools (Oleson et al., 2013). Each grid cell is covered by different land-use classes. Each class has its own set of plant functional types (PFTs) and soil columns. Vegetation is described by 15 different PFTs which either follow the C3 or C4 photosynthesis pathway. Twenty carbon (C) pools per PFT store C in vegetation. Decomposition of fresh litter material into progressively more recalcitrant forms of soil organic matter is formulated as a cascade of transformations between decomposing coarse woody debris, three litter, and three soil organic matter pools. These pools are vertically resolved by 10 layers over a depth of 3.8 m. Unlike in POP2, ^{14}C fractionation is not explicitly considered and CLM carries fractionation-corrected ^{14}C. The $^{14}C/C$ standard ratio is set to 10^{-12} in CLM5.0. Model results in gram-^{14}C are converted by multiplication with $1.176 \cdot 14/12.011 = 1.3707$ to compute ^{14}C inventories with 1.176 representing the ratio between the real and the model standard ratio, and 14 and 12.011 g/mol the molar mass of ^{14}C and C, respectively. ^{14}C decays in CLM5.0 with a half-life of 5,730 years.

2.3. Setup of Simulations

Eight simulations were performed. These include a spin-up (SPIN), a simulation over the historical period 1850 to 2015 (HIST) and an associated 165-year control run (CTRL) for both the land biosphere (LN) and the ocean-sea ice components (OC) with NYF. In addition, POP2 was run with an alternative climate forcing (JRA-55) over the historical period and in a corresponding control.

Spin-up and control runs were forced with 1,850 conditions for atmospheric CO_2 (284.7 ppm), $\delta^{13}C$ (−6.61‰), and $\Delta^{14}C$; prescribed atmospheric $\Delta^{14}C$ is distinguished between three latitudinal bands (>30°N: −2.3‰; 30°S–30°N: −4.0‰; and <30°S: –5.8‰) following Graven et al. (2017). The historical period simulation is forced with prescribed, transient atmospheric CO_2, $\delta^{13}C$, and $\Delta^{14}C$ following Meinshausen et al. (2017) and Graven et al. (2017).

In the code provided by the National Centre for Atmospheric Research (NCAR), atmospheric ^{14}C boundary values are read from input files. However, atmospheric boundary values are expected in units of $\delta^{14}C$ for the ^{14}C tracer in POP2, whereas atmospheric boundary values are expected in units of $\Delta^{14}C$ for the abiotic ^{14}C tracer in POP2 and by CLM5. We revised the code to account for this difference between $\delta^{14}C$ and $\Delta^{14}C$; the difference is around 37‰ ($2 \cdot (\delta^{13}C + 25) \approx 2 \cdot (-6.6 + 25)$) for preindustrial conditions.

CLM5 was forced with climate data from the Global Soil Wetness Project (Dirmeyer et al., 2006) which provides data from 1901 onwards. Spin-up (SPIN_LN), control simulation (CTRL_LN), and the first 50 years of the historical period simulation (HIST_LN) were forced by repeatedly prescribing the data for the period 1901 to 1920. The data for 1901 to 2015 were prescribed for the same period in HIST_LN. Land use is prescribed following the Land Use Harmonized version 2 data set (Hurtt et al., 2020). The specific setups, that is, the "compsets" provided by NCAR, are I1850Clm50BgcCrop for SPIN_LN and CTRL_LN and IHistClm50BgcCrop for HIST_LN.

POP2 was coupled to data models as in Jahn et al. (2015). Repeated NYF (Large and Yeager (2009)) from the Coordinated Ocean Research Experiments (CORE.v2) is applied during simulation SPIN_OC, CTRL_OC, and HIST_OC; NYF was also used by Jahn et al. (2015) and by the Ocean Model Intercomparison Project (Griffies et al., 2016). The low salinity bias in the subtropical-polar frontal zone simulated by the coupled CESM (Terhaar et al., 2021) is not present in our POP2 simulations; the mean salinity in the area south of 35°S is 0.08 g/kg higher in POP2 than deduced from the World Ocean Atlas. Climate data from the Japanese Reanalysis project (JRA-55, Kobayashi et al. (2015)) were used in a sensitivity simulation over the historical period (HIST_OC_JRA) and a corresponding control run (CTRL_OC_JRA); JRA-55 forcing was applied by some ocean models in the analyses of the Global Carbon Project (Friedlingstein et al., 2020). NYF data are repeated annually. The JRA-55 data cover the period from 1958 onwards. The JRA-55 data capture the influence of global warming while allowing us to prescribe a relatively constant climate in CTRL_OC_JRA and for the pre-1958 period in HIST_OC_JRA. Specifically, the first 20 years of JRA-55 (1958–1977) are applied repeatedly in the simulations CTRL_OC_JRA. Similarly, the first 20 years of JRA-55 data are applied repeatedly during the years 1850–1957 in HIST_OC_JRA, followed by the JRA-55 data for the post-1958 period. The global mean surface air temperature in JRA-55 varies within ±0.2°C in the control and the pre-1958 period of HIST_OC_JRA. This is followed by global warming of about 0.7°C over the period 1958 to 2015, mainly realized after 1989. As starting points in our setup, the compset G1850ECO was used for SPIN_OC and the compset G1850ECOIAF for CTRL_OC and for HIST_OC.

SPIN_LN was started using the initial files downloaded from NCAR (clmi.I1850Clm50BgcCrop.1366-01−01.0.9 x 1.25_gx1v6_simyr1850_c171213.nc: https://svn-ccsm-inputdata.cgd.ucar.edu/trunk/inputdata/lnd/clm2/initdata_map/) and run for 750 years. CTRL_LN and HIST_LN were continued from the end of SPIN_LN. The remaining model drifts in global carbon and radiocarbon are small after the SPIN_LN. Global vegetation carbon remains constant and the global soil carbon inventory changes by less than 1 GtC or about 0.5‰ over the control simulation. $\Delta^{14}C$ of vegetation carbon remains constant during the control CTRL_LN. Drift in $\Delta^{14}C$ are typically modest for soil carbon (<±2‰/century, except in northern Siberia and Canada and parts of the Sahara, where $\Delta^{14}C$ of soil carbon shows a substantial drift as these soils continue to age. The total ecosystem ^{14}C inventory decreases from 251 kmol to about 249 kmol over the control simulation. SPIN_LN required 9 days of "continuous" calculations using 30 nodes on the Cray XC40 system of the Swiss National Supercomputing Centre.

SPIN_OC was started using the initial files downloaded from NCAR (case: b.e21.B1850.f09_g17.CMIP6-piControl.001; https://svn-cesm2-expdb.cgd.ucar.edu/public/b.e21.B1850.f09_g17.CMIP6-esm-piControl.001) and run for 1,350 years. Initial values for ^{14}C and ^{13}C are missing in the files from NCAR and these missing values were specified as follows. $\delta^{13}C$ of DIC was prescribed following the gridded, observation-based preindustrial distribution of Eide et al. (2017); $\delta^{13}C$ values for the top 200 m are missing in the Eide et al. data and were set to the values at 200 m depth. $\delta^{13}C$ of DOC is set to −20‰. ^{14}C of DIC is initialized using the information for abiotic $\Delta^{14}C$ in the NCAR initial files. We assume $\delta^{13}C(DIC) = 0$ to set $\delta^{14}C_{biotic} = (\Delta^{14}C_{abiotic} + 50)/0.95$. $\Delta^{14}C$ of DOC is set to −100‰. SPIN_OC was stopped in year 675 to adjust the isotopic carbon pools of DIC and DOC to speed up equilibration. The difference in the isotopic pools between years 675 and 475 was added to the pools. In other words, the trend over years 475–675 was extrapolated for another 200 years. SPIN_OC was then continued for another 675 years with the updated isotopic concentrations. SPIN_OC and the POP2 industrial period simulations required 5 months (104 and 4 × 13 days) of "continuous" calculation using 12 nodes (the maximal possible configuration) on the Cray XC40.

Mean and deep ocean $\Delta^{14}C$ drift continuously toward more negative (older) values during SPIN_OC. These trends are indicative of an equilibration toward an older deep ocean. At the year 1350, the mean ocean trends in $\Delta^{14}C$ and in the absolute value of $\Delta^{14}C$ are −0.32‰ and 1.63‰ per century and horizontally average trends are between −5‰/century in the deep Pacific and +3‰/century in the upper Pacific and smaller for other basins (see Figures A1 and A2). Trends in abiotic and biotic $\Delta^{14}C$ are similar in magnitude and spatial distribution (Figures A1 and A2). Upper ocean trends are small in comparison to simulated anthropogenic changes. Nevertheless, we corrected the results of the historical period simulations using control runs. Thus, all results for bomb ^{14}C and bomb $\Delta^{14}C$ are not affected by trends. The results for deep ocean $\Delta^{14}C$ (Section 3.4) need to be considered with some caution.

2.4. Establishing the Global Budget of Excess ^{14}C

The transient evolution in the Earth system inventory of excess ^{14}C is estimated from the sum of the land and ocean excess ^{14}C inventories simulated by CLM5 and POP2 plus the tropospheric and stratospheric excess ^{14}C inventories estimated from measurements of $\Delta^{14}C(CO_2)$, $\delta^{13}C(CO_2)$, and CO_2 on atmospheric samples as described by Naegler and Levin (2009a).

The two excess ^{14}C production records of Naegler and Levin are estimated from the compilations of atomic bomb test explosions by Yang et al. (2000) or Rath (1988) and cover the bomb period up to 2004. These compilations are scaled to match an estimate of the total bomb ^{14}C inventory in the mid-1960s. The contribution of the ^{14}C release by the nuclear industry is included in these production records. The uncertainty in cumulative production up to 1980 is estimated to be around 6 kmol ^{14}C and the uncertainty in the stratospheric inventory to about 2–2.5 kmol ^{14}C, with additional smaller uncertainties associated with natural ^{14}C productivity, the release by the nuclear industry, and the tropospheric ^{14}C inventory (Naegler & Levin, 2006, 2009a). Any difference between the Earth system inventory and the cumulative production of excess ^{14}C represents an accumulated budget imbalance. Imbalances larger than uncertainties in the atmospheric and production data, point to a mismatch in simulated uptake of ^{14}C from the atmosphere by POP2 and CLM5.

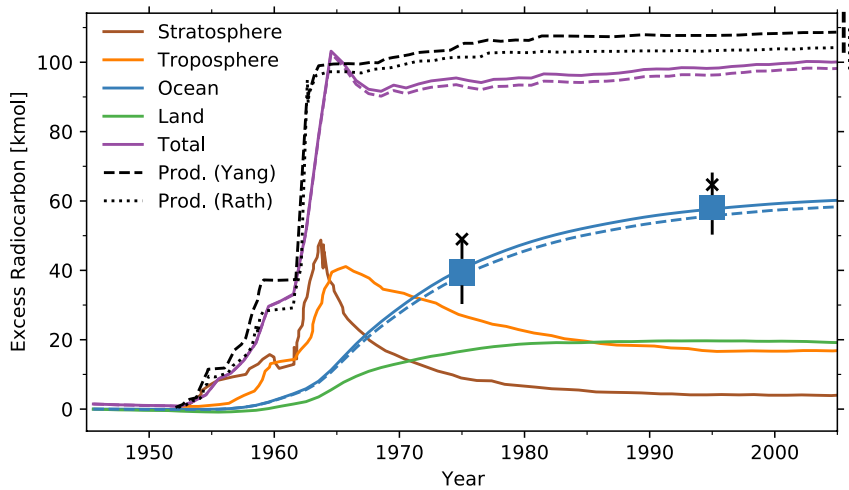

Figure 1. The Earth system budget of excess radiocarbon: observational estimates versus model results. The evolution of ^{14}C inventories are shown for the stratosphere (brown), troposphere (orange), ocean (blue), and land biosphere (green). Their total (magenta) is compared to two estimates of the excess ^{14}C production (black; dotted, dashed; with uncertainty ranges indicated by vertical lines). Data for the ocean and land biosphere are from simulations with POP2 and CLM5.0. Dashed blue and dashed magenta show results obtained with the JRA-55 instead of Normal Year Forcing in POP2. The ocean bomb ^{14}C inventories simulated by Jahn et al. (2015) are indicated by crosses. All other data are from Naegler and Levin (2009a). The range of best estimates (Key et al., 2004; Müller et al., 2008; Peacock, 2004; Sweeney et al., 2007) for the ocean inventory for 1975 and 1995 is given by the filled box and the bar represents the overall uncertainty of these estimates as summarized by Naegler and Levin (2009b). Production records are extrapolated from 2004 to 2010 assuming a constant trend.

3. Results

3.1. The Global Budget of Bomb ^{14}C

We first address the Earth system budget of bomb ^{14}C to evaluate the combined bomb ^{14}C model flux to the ocean and land. The change in the Earth system ^{14}C inventory is generally lower than estimates of the bomb ^{14}C production (magenta vs. black lines in Figure 1).

Both cumulative production records show a steep increase to 96–99 kmol until 1963, when the bomb-test ban treaty was set in place, followed by a modest increase of 7 kmol until 1980, and near-constant values after 1980. The estimate based on Rath remains around 4 kmol lower than the estimate based on Yang after 1963.

The stratospheric and tropospheric bomb inventory strongly increased in the 1950s to peak at 49 kmol in 1963 and 41 kmol in 1965. Afterward, the stratospheric inventory declined steeply, to 14 kmol in 1970 and 4 kmol in 2005, while the tropospheric inventory shows a more gradual decline to 17 kmol in 2005. Modeled land and ocean uptake of bomb ^{14}C are largest in the 1960s. The land inventory is 14 kmol in 1970, further increases to 19 kmol in 1980 and remains roughly stable thereafter. The ocean inventory is 30 kmol in 1970, further increases to 48 kmol in 1980 and reaches 59 kmol in 2000. The modeled inventory is slightly lower when POP2 is forced with the JRA-55 instead of the NYF; the difference between the two simulations is 1.9–2.0 kmol from 1974 onward.

The total Earth system inventory of excess ^{14}C reproduces the rapid initial increase in cumulative production of around 100 kmol ^{14}C, though with a delay of a few years. The inferred Earth system inventory peaks in 1964 and unrealistically declines in the next 3 years by about 10% from 103 to 92 kmol. This is in contrast to the cumulative production records that show little changes in this period. Afterward, the inventory follows the evolution of the cumulative production records, albeit at a lower absolute value. The combined bomb ^{14}C inventory shows an offset of 4–7 kmol to the cumulative production record based on Rath and of about 9 kmol to the record based on Yang during the period 1970 to 2005. In this period, the change in cumulative production (5–7 kmol) and the change in the Earth system inventory (7.5 kmol) remain relatively small and comparable, though there remain some differences in the evolution of these records. Thus, the budget imbalance mainly accrues before 1970. The accumulated budget imbalance of 4–7 kmol (Rath) and of about 9 kmol (Yang) is also similar or larger than the uncertainty in the cumulative production record of 6 kmol.

The differences between the cumulative ^{14}C production records and the Earth system inventory estimates suggest that the simulated uptake of excess ^{14}C from the atmosphere is underestimated. This is primarily the case during the 1960s when simulated ocean and land uptake is the largest. A too low combined uptake by POP2 and CLM5 in the 1960s could explain the delay in increase of the Earth system inventory estimates (magenta lines in Figure 1) relative to the cumulative ^{14}C production estimates (black lines in Figure 1) in the early 1960s. It could also explain the offset between the Earth system inventory and the production records after 1970 (magenta vs. black in Figure 1).

The inferred decline in the Earth system inventory of 11 kmol between 1964 and 1967 (Figure 1 magenta line) is infeasible due to mass conservation. Low ^{14}C uptake by CLM5 and POP2 or a bias in the observational atmospheric inventory change must be responsible for the decline. A doubling of the simulated ocean uptake would be needed to avoid the decline. Such a substantial upward revision would not be compatible with marine ^{14}C observations because modeled and observation-inferred bomb ^{14}C inventories closely agree and uncertainties in observational estimates are about 20% (Figure 1 blue symbols and line). Simulated land uptake amounts to five kmol only over these three years. NPP in CLM5 is around 50 GtC yr^{-1} and within the range of 41–64 GtC yr^{-1} estimated by Naegler and Levin (2009b). A systematic bias of more than 45 GtC yr^{-1} in mean NPP or an anomalous NPP flux of more than 20 GtC in each of the 3 years would be required for a ^{14}C uptake of 11 kmol. Such biases or variations in NPP are unrealistic. The prescribed atmospheric inventory decreases by 18 kmol from 1964 to 1967. Most of this decrease is realized in the stratosphere, where sampling is sparse and ^{14}C variations are large. However, the uncertainty (2–2.5 kmol) given for the stratospheric inventory data (Naegler & Levin, 2006, 2009a) are too small to account for 11 kmol. A scenario toward avoiding the decline might combine a downward revision of the stratospheric decrease, and an upward revision of modeled CLM5 land biosphere uptake and, perhaps to a lesser extent, of POP2 ocean uptake. The inferred decline in the Earth system inventory provides further evidence for a low bias in modeled ^{14}C uptake during the 1960s. Importantly, this evidence is independent of the production records and their uncertainties. In summary, the combined uptake by POP2 and CLM5 is too low during the 1960s, while the combined cumulative uptake over the period 1970–2005 is consistent with production estimates and atmospheric data.

3.2. The Ocean Bomb ^{14}C Inventory

The global ocean bomb ^{14}C inventory simulated by POP2 agrees well with observation-based estimates (Figure 1 blue line vs. symbols). POP2, driven by NYF, simulates an ocean inventory of 41.3 kmol in 1975 and 57.9 kmol in 1995. These estimates are well within the range of recent central estimates of the ocean's excess ^{14}C inventory of 36–44 kmol (overall uncertainty range: 30.3–49.3 kmol) for 1975 (Müller et al., 2008; Peacock, 2004; Sweeney et al., 2007) and 54.5–62 kmol (overall uncertainty range: 52–68 kmol) for 1995 (Müller et al., 2008; Peacock, 2004; Sweeney et al., 2007) and close to the ranges given by Naegler and Levin (2009a) of 42.0–46 kmol for 1975 and of 57.1–62.8 kmol for 1995. This good agreement between POP2 and observational estimates suggests that the budget imbalances discussed in the previous section are likely not primarily caused by too low modeled ocean uptake, but rather linked to too low uptake by the land biosphere.

The good agreement between the observation-inferred inventories and POP2 results supports the representation and time scales of air-sea gas transfer and surface-to-thermocline transport on the global scale for POP2 with NYF as well as JRA-55 forcing. The air-sea flux of bomb ^{14}C is given by the piston velocity multiplied by the perturbed air-sea gradient in dissolved $^{14}CO_2$ (Equation 1). The global ocean uptake of bomb ^{14}C before the first global survey of ^{14}C by the Geochemical Ocean Section Study (GEOSECS, 1972 to 1978) primarily depends on the magnitude of the piston velocity, whereas uncertain ocean transport has a marginal influence on the large air-sea $^{14}CO_2$ gradient during the time of the bomb peak (Müller et al., 2008; Siegenthaler, 1989). Thus, the GEOSECS bomb ^{14}C data provide a particularly strong constraint on the piston velocity. On the other hand, uncertainties in the overturning time scales within the ocean become important for the modeled ^{14}C uptake during more recent decades and the model inventory in 1995 (Graven et al., 2012; Müller et al., 2008).

Regionally, the highest column inventories of bomb ^{14}C are simulated in the North Atlantic (Figure 2). Column inventories are also high in the mid-latitude Southern Hemisphere, where Antarctic Intermediate Water and Subantarctic Mode Water (Talley, 2013) efficiently transports excess ^{14}C to depth. Column inventories are low in the tropical upwelling regions, around Antarctica, and in the northern North Pacific.

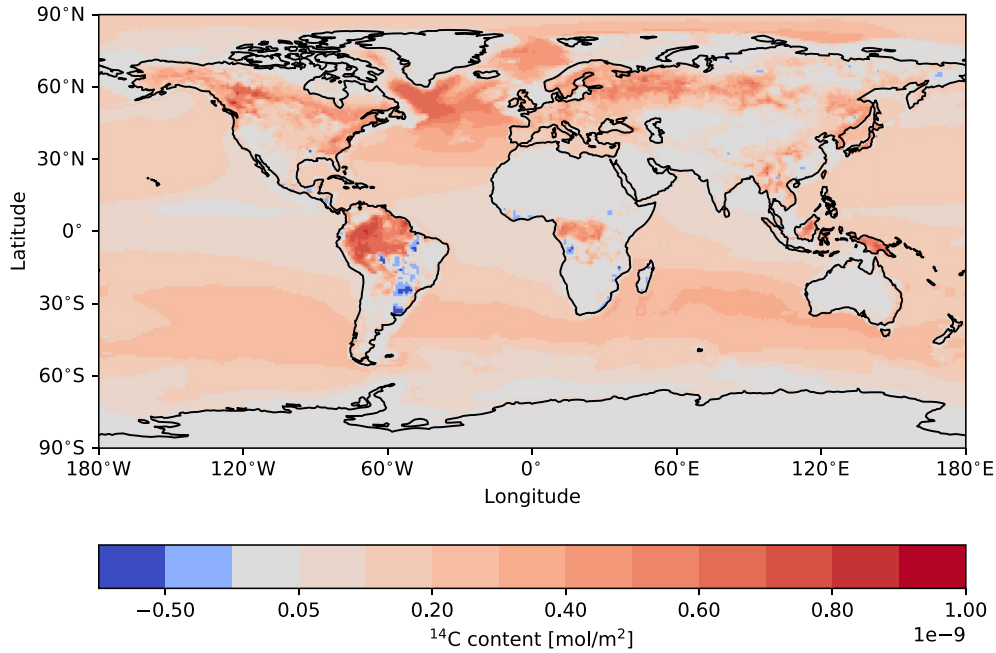

Figure 2. Changes in the ^{14}C column inventory in the ocean and on land from 1945 to 1995 simulated by Parallel Ocean Model version 2 with Normal Year Forcing (HIST_OC and CTRL_OC) and Community Land Model, version 5.0 (HIST_LN and CTR_LN).

3.3. Bomb ^{14}C in the CLM5 Land Biosphere

CLM5 simulates a terrestrial carbon release of 71 GtC over the period from 1850 to 1970 (Figure 3a). Land-use emissions are larger than sink fluxes in this period. Afterward, the model simulates a terrestrial carbon sink of 48 GtC until 2010. These changes are mainly driven by changes in vegetation carbon. Soil carbon (difference between black and green line in Figure 3a) decreased by about 5 GtC until 1970 and increased by 16 GtC from 1970 to 2010.

The simulated global land biosphere turned from a ^{14}C source into a sink around 1960 (Figure 3b). The CLM5 land biosphere released ^{14}C in the nineteenth and early twentieth century due to the loss of carbon, discussed in the previous paragraph, and the slight decrease in atmospheric $\Delta^{14}C$ (Figure 3d, red lines) and gained ^{14}C after 1960, mainly in response to the atmospheric bomb $\Delta^{14}C$ peak (Figure 3d). Vegetation lost 5.8 kmol of ^{14}C between 1850 and 1960, gained about 10 kmol in the next 20 years and its ^{14}C inventory remained stable thereafter. The soil ^{14}C inventory changed little (−0.26 kmol) until 1960, increased by 8.1 kmol to peak around 1995, followed by a slight decline.

Most of the land uptake of excess ^{14}C is by forest ecosystems (Figure 2). Typical bomb ^{14}C column inventories are around 1×10^{-9} mol ^{14}C m^{-2} in forested areas, and of similar magnitude as the column inventories in the northern North Atlantic. Deforestation caused local reductions in ^{14}C inventories over the bomb period in several regions, including Brazil, tropical Africa, and East Asia (Figure 2).

The bomb ^{14}C inventory simulated by CLM5 is below the lower bound of the range constructed by Naegler and Levin before 1990 (Figure 3b, right *y*-axis, black line vs. gray line and shading). It is 5.3 and 5.5 kmol lower than the reference scenario of Naegler and Levin in 1970 and 1985, respectively. These results imply that the cumulative uptake of bomb ^{14}C until 1970 is underestimated by CLM5 by about 25%. A 5 kmol higher bomb ^{14}C uptake over 1945 to 1970 by CLM5 would also reconcile the imbalance in the Earth system budget discussed in Section 3.1 for the period after 1970.

Soil ^{14}C data suggest that modeled ^{14}C uptake by soils is high. Shi et al. (2020) report less negative $\Delta^{14}C$ and younger soil ages in CLM5 than measured in modern soils (He et al., 2016; Shi et al., 2020). In surface soils in 2000 CE, over 60% of the surface soil carbon in CLM5 had positive $\Delta^{14}C$ values compared with only about 14% of the carbon in the gridded global observational data set (Shi et al., 2020). Positive $\Delta^{14}C$ values must originate

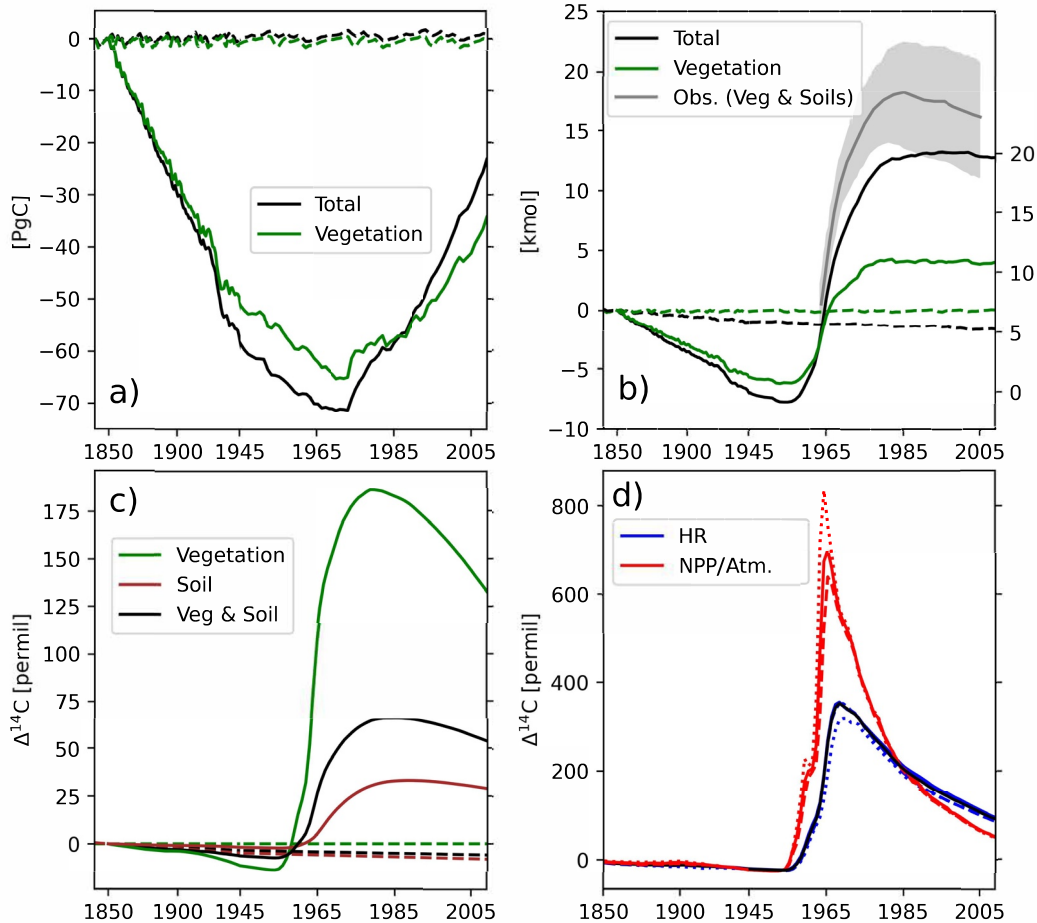

Figure 3. Changes in the global land biosphere simulated by Community Land Model, version 5 (CLM5). (a) Carbon inventory, (b) ^{14}C inventory (left *y*-axis), (c) mean $\Delta^{14}C$ of vegetation (green), soils (red), and vegetation and soils (black), and (d) mean $\Delta^{14}C$ of heterotrophic respiration (HR; blue) and net primary productivity (NPP) and tropospheric CO_2 ("Atm."; red) for three latitudinal belts (dotted: >30°N; solid: 30°S–30°N; and dash <30°S). The right *y*-axis in panel (b) refers to changes in the total (soil and vegetation) inventories of ^{14}C in kmol relative to 1945 and permits one to compare the ^{14}C inventories simulated by CLM5 (black) with the observation-inferred estimate of Naegler and Levin (2009a) (gray solid: their reference; shading: range spanned by their upper- and lowermost estimates). Dashed lines in panels (a–c) show changes in the control simulation as used to correct for model drift. Note the different *x*-axis scaling before and after 1945. In 1850, vegetation and total carbon inventories are 600 and 2,840 GtC; NPP is 42.3 GtC yr^{-1} and increases to 55.7 GtC yr^{-1} in 2015.

from the uptake of bomb ^{14}C. In other words, the higher than observed $\Delta^{14}C$ in surface soils suggests that the surface soils of CLM5 absorb too much bomb ^{14}C. Bringing simulated soil $\Delta^{14}C$ in agreement with soil $\Delta^{14}C$ observations, would probably lower bomb ^{14}C uptake by soils and thus widen the discrepancy between the bomb ^{14}C uptake simulated by CLM5 and the observational range given by Naegler and Levin (2009a). These considerations imply that the uptake of bomb ^{14}C by vegetation is too low.

A change in the inventory of carbon causes a corresponding change in the ^{14}C inventory. The release of carbon in the nineteenth and early twentieth century and the carbon uptake in the late twentieth century is in line with results from a deconvolution of the atmospheric CO_2 record (Friedlingstein et al., 2019; Joos et al., 1999). For the period 1970 to 2010, CLM5 yields a global land sink of about 48 GtC, while the Global Carbon Budget suggests a sink of 41 GtC. This difference in carbon translates into a small difference in the ^{14}C inventory of ~1 kmol ^{14}C when multiplied with the molar $^{14}C/C$ ratio of the atmosphere. However, independent evidence (Friedlingstein et al., 2019; Joos et al., 1999) suggests that the land biosphere turned into a sink already around 1940 and not only around 1970 as in CLM5. The land biosphere absorbed 6 ± 6 and 10 GtC during the period 1945 to 1970 according to the observation-based estimate of Joos et al. (1999) and the results from the Global Carbon Budget

(Friedlingstein et al., 2019), respectively. In contrast, CLM5 suggests a release of about 13 GtC in the same period. This difference between modeled and estimated carbon uptake of 19–23 GtC transfers in an additional uptake of ~2–3 kmol ^{14}C during the period 1945–1970. This additional ^{14}C would contribute to lower the discrepancy between model-based ^{14}C inventory and production estimates as discussed in Sections 3.1 and would bring CLM5 results in better agreement with the reference scenario for the land inventory of Naegler and Levin (2009a) (Figure 3b). Additional factors, for example, a larger NPP and carbon allocation to long-lived vegetation pools in CLM5, are needed to remove the discrepancy, as further discussed in Section 4.1.

The perturbation in isotopic disequilibrium between the major input and output fluxes, that is, the difference in $\Delta^{14}C$ of NPP and heterotrophic respiration, largely drives the net flux of bomb ^{14}C into the land biosphere (Joos & Bruno, 1998). $\Delta^{14}C$ of NPP equals $\Delta^{14}C$ of assimilated atmospheric CO_2 (Figure 3d, red lines). In contrast, $\Delta^{14}C$ of heterotrophic respiration represents the average $\Delta^{14}C$ of previously assimilated CO_2 which was transformed from organic C of plant tissues to litter and soil carbon, and, at time t, back to CO_2 by heterotrophic respiration. The $\Delta^{14}C$ signature of heterotrophic respiration follows the atmospheric $\Delta^{14}C$ forcing with a delay and with muted amplitude (Figure 3d). $\Delta^{14}C$ of heterotrophic respiration peaks at around 330‰ and a few years later than tropospheric $\Delta^{14}C$. It equals tropospheric $\Delta^{14}C$ around 1985 and remains above tropospheric $\Delta^{14}C$ thereafter. In turn, the isotopic disequilibrium between NPP and heterotrophic respiration (difference between red and black lines in Figure 3d) and the bomb uptake (slope of the black line in Figure 3b) are largest around 1965 and diminishes thereafter.

The changes in $\Delta^{14}C$ of vegetation and soils represent the integrated signal of bomb ^{14}C (and carbon) uptake. On a global average, their $\Delta^{14}C$ signatures peak around 1980 (Figure 3c), when the isotopic disequilibrium (Figure 3d) and bomb inventory changes (Figure 3b) have become small. The global average $\Delta^{14}C$ of vegetation declined from −5.4‰ to −18.7‰ from 1850 to 1955, increased in the next 25 years to peak around +180‰ and declined by about 50‰ until 2010. The global-average bomb $\Delta^{14}C$ signals in soil carbon is substantially smaller than in vegetation carbon and peak $\Delta^{14}C$ is further delayed. $\Delta^{14}C$ in soil carbon increased from around −137‰ to −102‰ from 1955 to 1990. These responses in $\Delta^{14}C$ are consistent with an increase in mean age (Bolin & Rodhe, 1973) from heterotrophic respiration, to vegetation carbon, and to soil carbon.

3.4. Distribution of Natural and Bomb $\Delta^{14}C$ in the Ocean

3.4.1. The Coral $\Delta^{14}C$ Records

Time-series data from corals and bivalves show a rapid $\Delta^{14}C$ increase during the 1960s in surface waters (Figure 4). Surface $\Delta^{14}C$ peak in the late 1960s and early 1970s, followed by a slow decline. The amplitudes in surface $\Delta^{14}C$ change between pre-bomb and peak values range between 85‰ and 250‰ (Figures 4k and 4f).

The model represents the pre-bomb (~1950) $\Delta^{14}C$ proxy data from corals and bivalves within the scatter of the proxy data in the surface North Atlantic (Figures 4b–4m), with some exceptions (Figures 4c–4e). Pre-bomb $\Delta^{14}C$ simulated by POP2 is typically about 10‰–15‰ lower than the $\Delta^{14}C$ data from the Pacific and the Indian Ocean (Figures 4o–4t). POP2 underestimates the measured increase in surface Δ14C during the bomb-test period at all locations. Deviations in peak surface $\Delta^{14}C$ range from a few permil to up to 75‰. The evolution of $\Delta^{14}C$ at depth is within the scatter of the available coral data at Bermuda (Figure 4e, gray) and the Bay of Biscay (Figure 4j) and underestimated at Grand Banks (Figure 4c). Peak $\Delta^{14}C$ values from the POP2 simulation with JRA-55 wind forcing are similar to those obtained with NYF at mid and high latitudes in the North Atlantic but typically lower than for NYF at Bermuda and Puerto Rico and in the low-latitude Pacific and Indian locations. $\Delta^{14}C$ at pre-bomb times and after 1990 are generally indistinguishable for the POP2 model setup with NYF (HIST_OC) versus the setup with JRA-55 (HIST_OC_JRA) forcing. The lower than observed pre-bomb and peak $\Delta^{14}C$ values in the low-latitude Indian and Pacific may point to too strong upwelling of thermocline waters in POP2 or too sluggish gas transfer at these locations.

3.4.2. Bomb $\Delta^{14}C$ in the Ocean

Next, we compare basin-mean profiles of simulated versus observation-derived bomb $\Delta^{14}C$(DIC) profiles for the WOCE era (Figure 5). The modeled bomb $\Delta^{14}C$ profiles under NYF and JRA-55 forcing show close agreement, with slightly lower values under JRA-55 than NYF forcing. The model values are substantially lower in the Atlantic and Pacific than estimated from observation, while the model-data agreement is reasonable in the Indian and

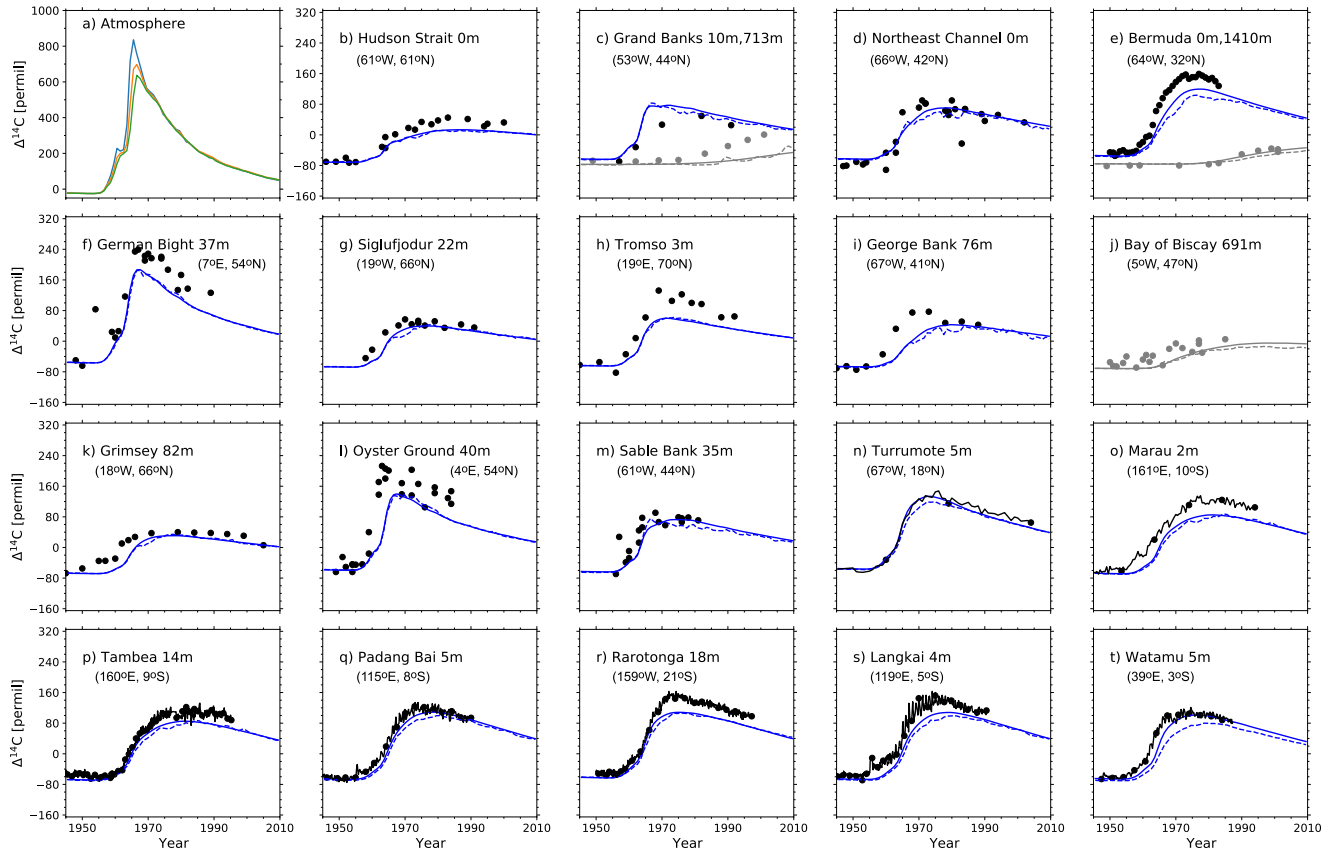

Figure 4. Simulated evolution of $\Delta^{14}C(DIC)$ by Parallel Ocean Model version 2 (solid and dashed lines) versus $\Delta^{14}C$ records from corals and bivalves (filled circles panels (b–m), filled circles with solid lines for high-resolution records panels (n–t)). Model results are for the simulation with Normal Year Forcing (solid) and JRA-55 (dashed) forcing and represent annual means from the grid cell including the sampling location and sampling depth (indicated in meters). Data and model results in the thermocline are shown in gray. Data are from the North Atlantic as compiled by Dentith et al. (2019), Puerto Rico, Turrumote Reef (Kilbourne et al., 2007), Solomon Islands, Marau (Schmidt et al., 2004), Solomon Islands, Tambea (Guilderson et al., 2004), Lombok Street, Padang Bai (Guilderson et al., 2009), Rarotonga (Guilderson et al., 2000), Langkawi, Makassar Strait (Fallon & Guilderson, 2008), and off the coast of Kenya, Watamu (Grumet et al., 2002). The atmospheric $\Delta^{14}C(CO_2)$ evolution is shown in panel (a) for the northern hemisphere (>30°N; blue), the tropics (orange), and the Southern Hemisphere (<30°S; green); note different *y*-axis scale.

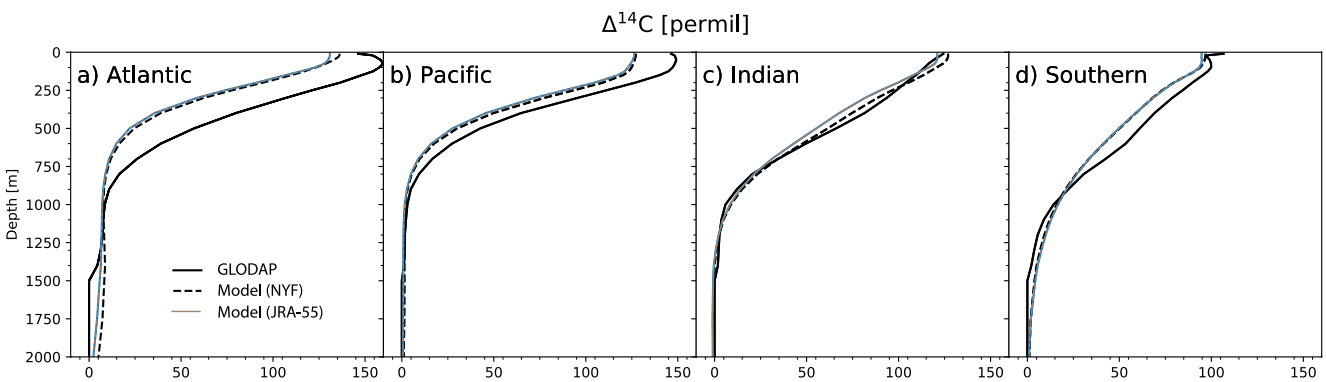

Figure 5. Simulated (black dash; gray) versus observation-based (black solid) basin-mean profiles of bomb $\Delta^{14}C(DIC)$. Model results are from the HIST_OC (dash) and the HIST_OC_JRA (gray) simulations and corrected for model drift. The Southern Ocean (panel (d)) includes the area south of 35°S and these areas are not included in the profiles for the Atlantic, Pacific, and Indian Ocean (panels (a–c)). The model is only sampled where Global Ocean Data Analysis Project (GLODAP) gridded data are available; the Arctic Ocean and some other smaller oceans are not covered by the GLODAP $\Delta^{14}C$ data. The model is sampled in 1982 in the North Atlantic and in 1988 in the South Atlantic and in 1995 in all other regions to account for the different measurement periods.

Southern Ocean with deviations of up to 10‰ (Figure 5). The model underestimates bomb $\Delta^{14}C$ at the surface in most regions in the Atlantic and the Pacific (not shown) and on average by almost 20‰. In the thermocline, these deviations become even larger in the Atlantic.

This underestimation is, at first glance, at odds with the good agreement between simulated and observation-based global ocean bomb ^{14}C inventories displayed in Figure 1. The original bomb ^{14}C inventory published by (Key et al., 2004) is 52.3 kmol and thus 3.6 and 5.6 kmol lower than simulated by POP2 (57.9 kmol in HIST_OC and 55.9 in HIST_OC_JRA) for the year 1995. However, this GLODAP bomb ^{14}C inventory has been corrected upwards to 63.6 kmol by (Naegler, 2009) by accounting for the increase in DIC and for missing areas (Naegler, 2009). In turn, this revised GLODAP-based global bomb ^{14}C estimate is now 11% higher than simulated under NYF and 14% higher than under JRA-55. Thus, simulated bomb $\Delta^{14}C$(DIC) and simulated global bomb ^{14}C inventory are both biased low relative to the GLODAP data product.

Increasing the rate of air-sea gas exchange in the Atlantic and Pacific would help to diminish the model bias relative to the GLODAP data and increase global bomb ^{14}C inventory and bomb $\Delta^{14}C$(DIC). Increasing air-sea exchange would also help to diminish the bias between the coral records and POP2 discussed in the previous subsection. A too slow surface-to-deep transport could potentially also cause biases in bomb inventory and $\Delta^{14}C$. However, earlier work shows good agreement between observed and simulated CFC-11 concentrations for POP2, indicating a good representation of upper ocean transport rates (Danabasoglu et al., 2009). Further, higher transport rates in the upper Atlantic and Pacific would tend to increase the model-data mismatch even more at the surface.

3.4.3. The Preindustrial Distribution of $\Delta^{14}C$ in the Ocean

We now turn to the preindustrial $\Delta^{14}C$(DIC) distribution in the ocean to investigate transport time scales in the deep-ocean. The comparison of observed versus simulated $\Delta^{14}C$(DIC) in the surface ocean (Figures 6 and 7) suggests that the air-sea gradient of $\Delta^{14}C$ is represented roughly in agreement with observational estimates. The global mean area-weighted surface ocean $\Delta^{14}C$ is 1.5‰ lower in the model (SPIN_OC; −67.94‰) than in the GLODAP data (−66.47‰). There is still a positive trend in most surface regions and of about 0.6‰ per century on global average at the end of SPIN_OC (Figure A1 and A2). The root mean square deviation between model and GLODAP data is 9‰. Surface $\Delta^{14}C$ is overestimated in parts of the Pacific and Indian sectors of the Southern Ocean and underestimated in the Atlantic sector (Figure 7). Surface $\Delta^{14}C$ is also underestimated in the northern North Atlantic and Pacific (Figure 7).

In contrast to the surface, $\Delta^{14}C$(DIC) is consistently underestimated in the deep ocean by POP2 (Figures 6 and 7). Below the surface, radioactive decay of ^{14}C acts as a sink process, and $\Delta^{14}C$ decreases along the flow path of a water mass. Basin-average differences between model and observational data are about 5‰ in the upper Atlantic and grow to about 45‰ in the deepest waters. This implies that the radiocarbon age of the deep Atlantic is overestimated by about 450 years. Even larger mean biases of around 70‰, or 770 years in age, are found at around 2,000 m in the Pacific, while mean biases are smaller and less than ∼25‰ (250 years) in the Indian and Southern Ocean. There is still a negative trend in $\Delta^{14}C$(DIC) below 3,000 m of order −2‰ per century at the end of SPIN_OC (Figure A1 and A2) and we expect that the data-model mismatch will even be larger at equilibrium. Ocean overturning and ventilation of the deep water masses are too sluggish in the POP2 model. This is a known model bias of POP2 as discussed by Jahn et al. (2015, and references therein) and also found in an ongoing ^{14}C-enabled simulation with the fully coupled CESM2 model with interactive atmosphere.

The sluggish circulation causes biases in biogeochemical tracers (Figure 6). The too-long residence time of deep waters causes a too-large accumulation of inorganic DIC and phosphate (P) released by organic matter remineralization, particularly in the Pacific. There, the basin-mean biases in DIC and P are up to 190 and 5 mmol m^{-3}, respectively. The trapping of excess P in the Pacific thermocline and deep Pacific leads to a depletion of P in the other basins and at the surface, as the P inventory is fixed in the model. Low biases in surface P are particularly pronounced in the northern Pacific, the Pacific equatorial region, and the Southern Ocean, with potential implications for primary productivity and organic matter export. These results suggest that observations of $\Delta^{14}C$, DIC, P, and other biogeochemical tracers provide useful constraints on deep ocean circulation.

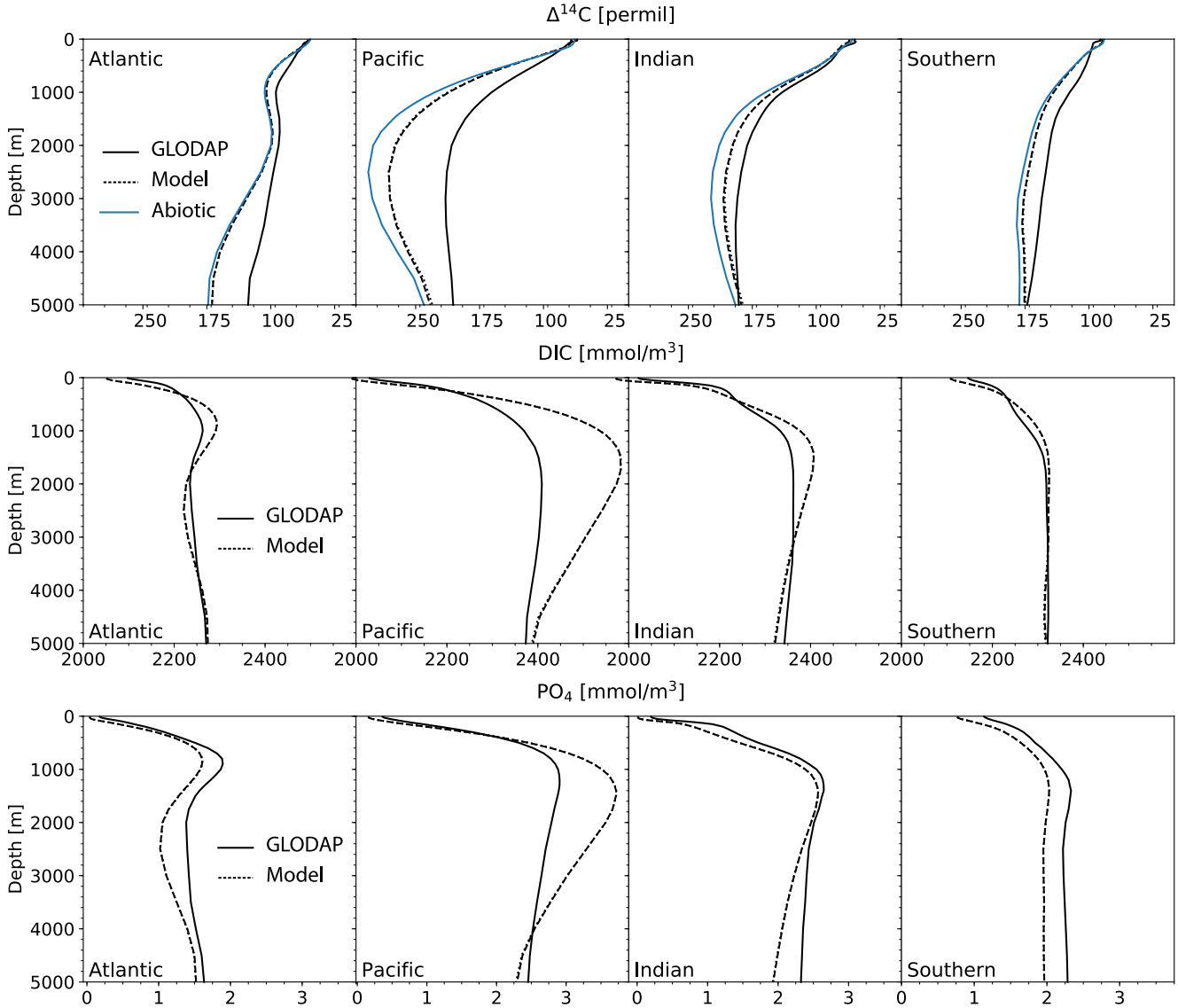

Figure 6. Simulated (black dash) versus observation-based (black solid) (Garcia et al., 2013; Key et al., 2004) basin-mean profiles of $\Delta^{14}C$(DIC), dissolved inorganic carbon, and PO_4 for the preindustrial period. The blue lines show the preindustrial model results for the abiotic radiocarbon tracer. The Southern Ocean includes the area south of 35°S and these areas are not included in the profiles for the Atlantic, Pacific, and Indian Ocean. For $\Delta^{14}C$, the model is only sampled where Global Ocean Data Analysis Project (GLODAP) gridded data are available; the Arctic Ocean and some other smaller oceans are not covered by the GLODAP $\Delta^{14}C$ data.

3.4.4. Abiotic Versus Biotic ^{14}C Tracers

Next, results for the abiotic formulation, neglecting fluxes between organic matter and DIC, are compared to the computationally demanding biotic formulation (blue vs. dashed line in Figure 6). Less negative $\Delta^{14}C$ in the biotic than in the abiotic simulations is expected in deep, nutrient-rich waters (Figure 6, bottom) as the remineralization of organic matter adds DIC with a relatively high $\Delta^{14}C$ to the DIC pool. Model drift in the deep ocean (Figure A1 and A2) affects the comparison and calls for caution, though abiotic and biotic $\Delta^{14}C$ were initialized to very similar values and differences between these tracers materialized during the spin-up (SPIN_OC). At the surface, model drift presents a small problem because surface biotic and abiotic $\Delta^{14}C$ are tied to the prescribed atmospheric ^{14}C by air-sea exchange. The basin-mean profiles in the upper thermocline and the entire Atlantic show close agreement between abiotic and biotic $\Delta^{14}C$. Mean $\Delta^{14}C$ differences in the Southern Ocean are relatively small, while substantial differences are simulated in the deep Indian and Pacific.

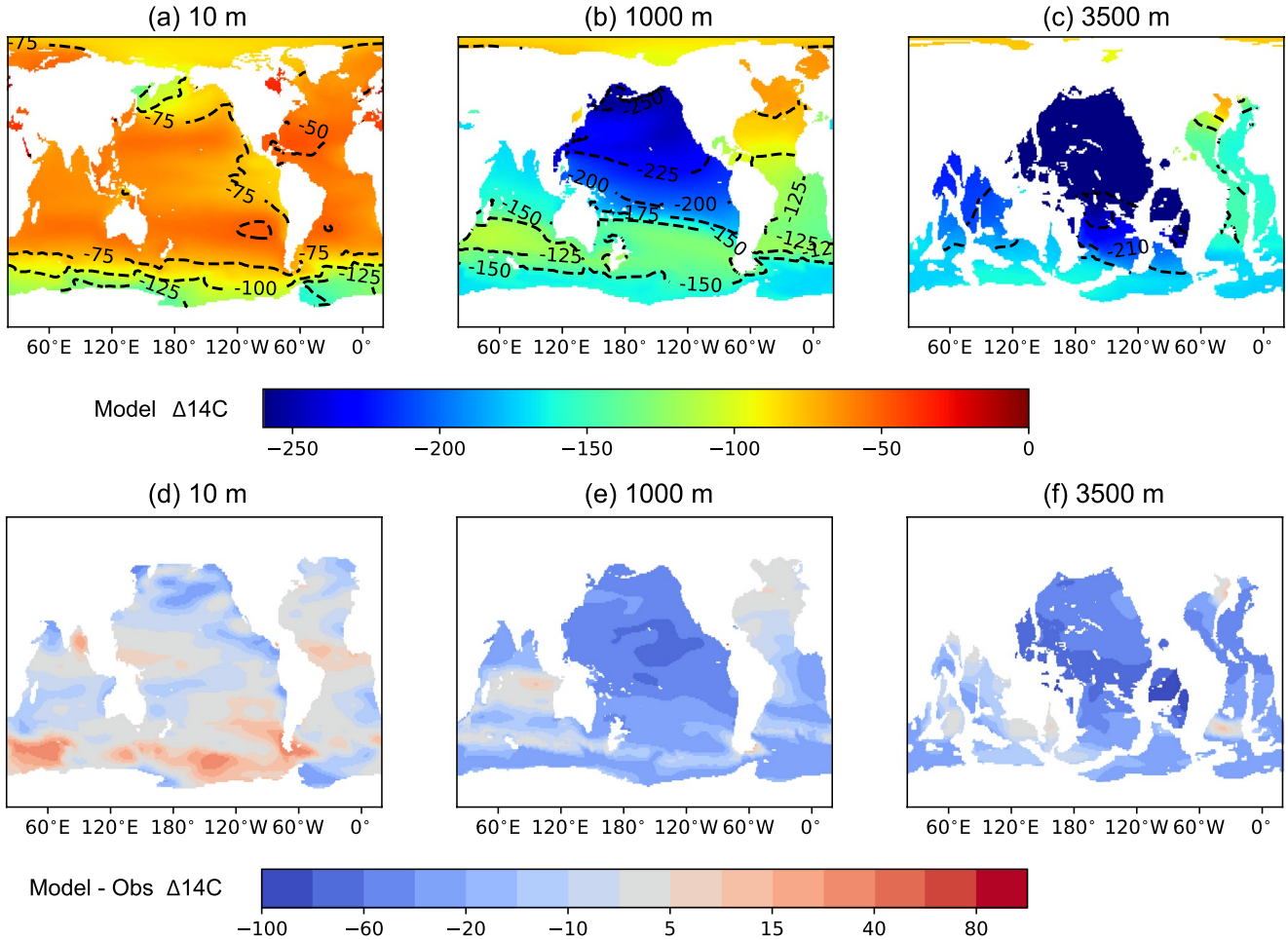

Figure 7. Simulated versus observation-based distribution of $\Delta^{14}C$(DIC) for the preindustrial period at the surface, 1,000 m, and at 3,500 m. Model results (top panels) are from the end of the spin-up simulation SPIN_OC. The lower panels show the difference of simulated $\Delta^{14}C$ minus observation-based $\Delta^{14}C$ (Key et al., 2004).

The good agreement in biotic and abiotic $\Delta^{14}C$ in the upper ocean and the Atlantic, as well as higher biotic than abiotic $\Delta^{14}C$ (Figure 6), is in contrast to the findings of Jahn et al. (2015). These authors show biotic $\Delta^{14}C$ to be around 40‰ lower than abiotic $\Delta^{14}C$ at the surface and for 1990 CE (their Figure 4). Biotic $\Delta^{14}C$ is also lower than abiotic $\Delta^{14}C$ throughout the water column. It appears that the large difference between biotic and abiotic $\Delta^{14}C$ presented by Jahn et al. is explained by their atmospheric boundary condition for the biotic tracer. Too low biotic $\Delta^{14}C$ values are simulated when inadvertently prescribing atmospheric $\Delta^{14}C$ instead of atmospheric $\delta^{14}C$ to the biotic ^{14}C tracer. The difference between $\delta^{14}C$ and $\Delta^{14}C$ (Equation 1) is about 37‰ ($2 \times (\delta^{13}C + 25)$) for a preindustrial $\delta^{13}C$ of −6.379‰ as used by Jahn et al. (2015).

4. Discussion

The inventory of bomb ^{14}C in CLM5 remains below the lower uncertainty bound of the observational estimate of Naegler and Levin (2009a) for the period 1963–1990 (Figure 3b). Naegler and Levin considered uncertainties in ocean uptake, the stratospheric and tropospheric inventory, and the production rates of bomb ^{14}C to derive their uncertainty bound for the land biosphere inventory. This estimate and the Earth system budget of bomb ^{14}C both rely on the same bomb ^{14}C production records and atmospheric inventory data and therefore share some common uncertainties. The results suggest that CLM5 simulates a too-low uptake of bomb ^{14}C, mainly in the 1960s, and that this low uptake explains, at least partly, the imbalances in the Earth system budget and the deviation between simulated and observation-derived land biosphere inventory of bomb ^{14}C.

CLM5 underestimates the net carbon sink on land during the period 1945–1970 and this translates into a deficit in ^{14}C uptake of about 2–3 kmol. Thus, a better representation of the net carbon sink in CLM5 would potentially tend to narrow but not close the gap between the modeled and observation-based bomb ^{14}C inventory of the land biosphere.

The CLM5 results show that forests are the largest sink of bomb ^{14}C in the land biosphere (Figure 2). This carbon reservoir is of high importance for the land sink of anthropogenic carbon (Arora et al., 2020). We argue that too low bomb ^{14}C sequestration by wood in CLM5 is mainly responsible for the low bias of the simulated global land biosphere bomb ^{14}C inventory. Grasses and shrub ecosystems have a small above-ground carbon inventory. In turn, the vegetation of these systems cannot sequester much bomb ^{14}C. Similarly, the short-turnover time and the low carbon inventory of leaves and needles and fine roots do restrict their potential for bomb ^{14}C sequestration. Soils could potentially sequester a lot of bomb ^{14}C given their large carbon stocks and slow overturning. However, $\Delta^{14}C$ in modern soils is consistently overestimated in CLM5 (Shi et al., 2020), suggesting rather a too large and not a too low uptake of bomb ^{14}C by soils in CLM5. Taken together, we conclude that the uptake of ^{14}C by forest vegetation is biased low. In turn, the carbon fluxes allocated to wood and/or the overturning time scales of wood carbon in forests are probably biased low in CLM5. This could potentially be associated with a low bias in NPP of forest ecosystems.

The low bias in bomb ^{14}C uptake could imply a bias in the sequestration of anthropogenic carbon by forest vegetation. To illustrate the magnitude of the bias, we attempt to quantify the mismatch in the bomb ^{14}C inventory of vegetation. CLM5 underestimates the peak in the bomb ^{14}C inventory of both vegetation and soils by about 5 kmol (range: 1.5–9 kmol; thin line and shading vs. thick black line in Figure 3b). Together with the high soil $\Delta^{14}C$ (Shi et al., 2020) discussed above, this implies that the bomb ^{14}C inventory of vegetation is underestimated by at least the same amount. In comparison, simulated peak uptake by vegetation is 11 kmol (Figure 3b). In other words, bomb ^{14}C uptake by vegetation is underestimated significantly, by more than 31% (12%–45%). Future work may attempt to remove the bias in the bomb-^{14}C inventory of vegetation to constrain and better represent past and future uptake of anthropogenic carbon.

Turning to the ocean, the agreement of POP2 results with the observation-based bomb ^{14}C inventories (Figure 1, blue curves and symbols) supports using the NYF and JRA-55 wind products together with the scaling of Wanninkhof (2014). Jahn et al. (2015) applied a 24% larger coefficient (0.31 cm hr^{-1} m^{-2} s^{-2}) than used here and NYF. Correspondingly, their simulated bomb ^{14}C inventory is at the upper end of the observational range (Figure 1, black x vs. blue symbol with error bar).

Differences in circulation under NYF compared to JRA-55 forcing may cause differences in $\Delta^{14}C$ and bomb ^{14}C column inventories. It remains difficult to link the relatively small differences in local bomb Δ ^{14}C and local column bomb ^{14}C inventories (Figure B1) to differences in ocean dynamics versus differences in piston velocities. $\Delta^{14}C$ differences between the two control simulations with NYF (CTRL_OC) and JRA-55 forcing (CTRL_OC_JRA) are both positive and negative and typically less than 4‰ in 1995 in the upper Atlantic and Southern Ocean. Somewhat larger anomalies are found in the Pacific thermocline around 15°N and 30°S (not shown). Differences in bomb ^{14}C column inventories are small but differences in wind speed/piston velocity are substantial in the low latitude Pacific and Atlantic (Figure B1), pointing to the important influence of ocean circulation for local bomb $\Delta^{14}C$ and column inventories in these specific regions.

Our results suggest in agreement with earlier findings (Jahn et al., 2015, and references therein) that deep ocean ventilation is too slow in POP2 with implications for biogeochemical tracer distributions (Figure 6) and climate projections. The too-long residence time of deep ocean waters in POP2 leads to a too large accumulation of biogeochemical tracers and oxygen depletion by organic matter remineralization. Notably, DIC and phosphate are biased high compared to observations (Garcia et al., 2018; Key et al., 2004) by up to 400 and 3 mmol m^{-3} in the deep Pacific. The large bias in deep ocean ventilation likely affects projections of atmospheric CO_2 and global warming, ocean heat uptake and sea-level rise, and ocean acidification and deoxygenation. In particular, we expect a too slow uptake of ocean heat and carbon by the deep ocean in climate projections. In turn, atmospheric CO_2 and global warming would be overestimated and thermal expansion of deep waters, contributing to sea-level rise, delayed. The bias in deep ocean $\Delta^{14}C$ suggests that the representation of deep ocean circulation and overturning time scales should be improved to improve the representation of biogeochemical tracers and Earth system projections.

5. Conclusions

The analysis of bomb- and naturally produced ^{14}C provides insight into the timescales and processes governing the global carbon cycle, atmospheric CO_2, and climate. Our results suggest that the carbon flux allocated to wood and/or the overturning time scales of wood carbon in forests are biased in the land biosphere model CLM5 and that the deep ocean ventilation is too slow in the POP2 ocean model. Modeled global ocean bomb ^{14}C inventories are consistent with observational estimates for the air-sea gas exchange piston velocity parameterization of Wanninkhof (2014) combined with NYF and JRA-55 wind data.

Future efforts may be directed to adapt CLM5 and POP2 formulations to lower the identified biases in CLM5 and POP2. A longer ^{14}C-enabled spin-up of POP2 would be desirable to reduce the substantial model drift and allow for better quantitative statements regarding deep ocean ventilation. Another task is to simulate ^{14}C in fully coupled Earth system models either with prescribed atmospheric $\Delta^{14}C$ boundary conditions, as done in this study, or with prescribed ^{14}C sources (Kovaltsov et al., 2012; Masarik & Beer, 2009; Naegler & Levin, 2009a; Roth & Joos, 2013) and freely evolving CO_2 and $\Delta^{14}C(CO_2)$ to constrain exchange time scales for improved CO_2 and climate projections.

Appendix A: Model Drift

Figures A1 and A2 show the trends in abiotic and biotic $\Delta^{14}C$ of DIC, evaluated at the end of the spin-up of POP2.

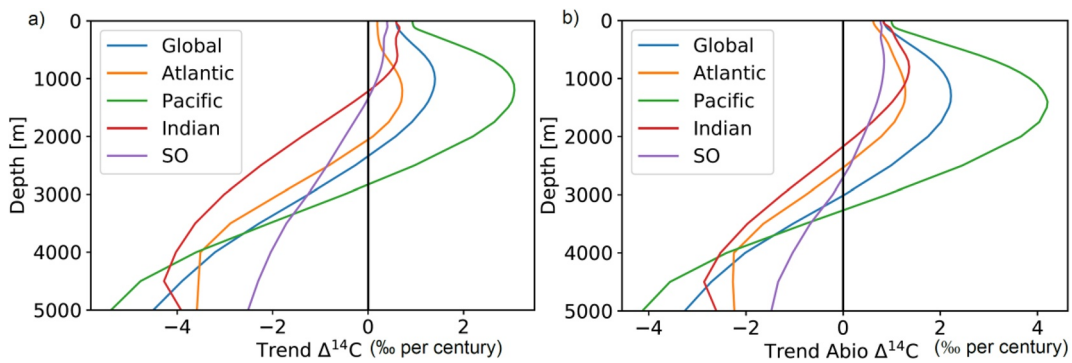

Figure A1. Basin-mean trends in (a) biotic and (b) abiotic $\Delta^{14}C$ in permil per century.

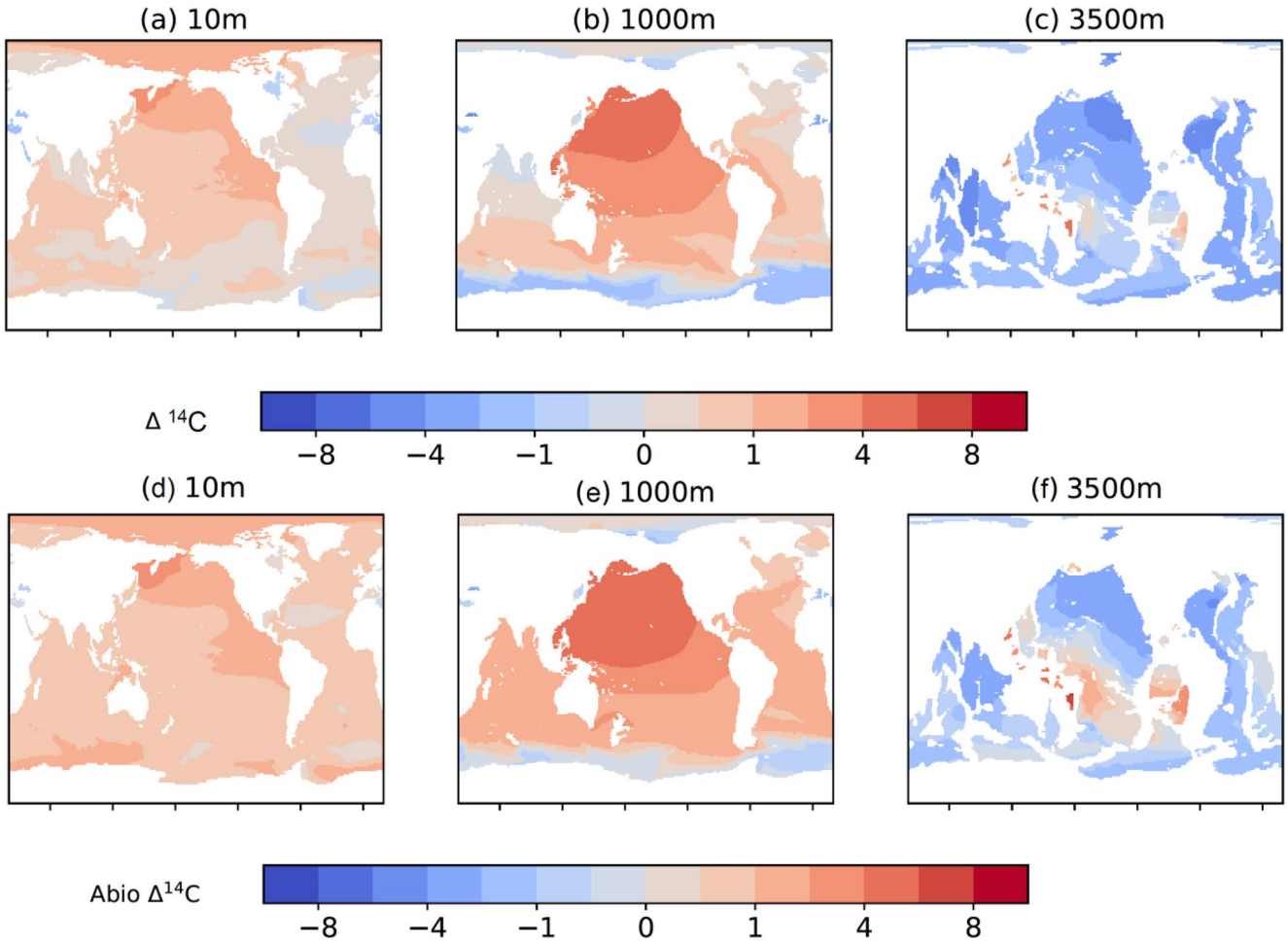

Figure A2. Trends in biotic (a–c) and abiotic (d–f) $\Delta^{14}C$ in permil per century at different depth levels.

Appendix B: Wind Speed and NYF Versus JRA-55

Figure B1 highlights the spatial differences in the prescribed annual mean of the wind speed squared at 10 m and bomb ^{14}C column inventory between the POP2 simulations with Normal Year versus JRA-55 forcing.

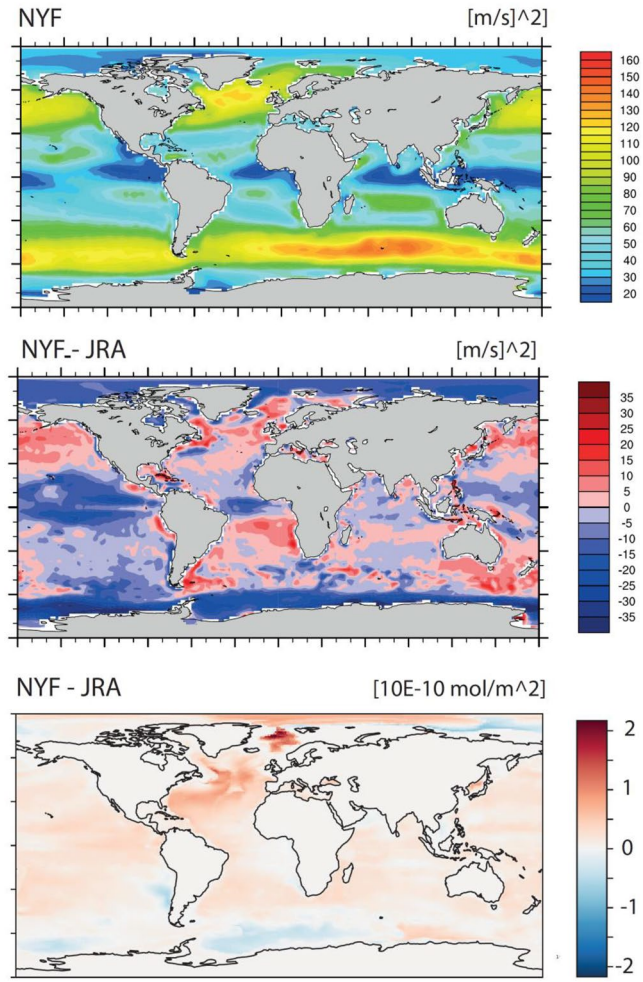

Figure B1. Annual mean of the wind speed squared at 10 m as used to compute the air-sea gas exchange piston velocity for (top) the Normal Year Forcing (NYF), (middle) the difference between NYF minus Japanese Reanalysis (JRA-55) wind data, and the difference in column bomb ^{14}C inventory between the simulations with NYF and JRA-55 forcings. JRA-55 winds are averaged over the period from 1958 to 1977; NYF data cover 1 year. Global mean values are 62.70 and 67.65 $m^2\ s^{-2}$ (1958–1977; range of annual values: 66.69–68.78 $m^2\ s^{-2}$) for NYF and JRA-55, respectively.

Data Availability Statement

The model code for CESM2 is publicly available: https://www.cesm.ucar.edu/models/cesm2/release_download.html. ^{14}C records are available on the NOAA data server: https://www1.ncdc.noaa.gov/pub/data/paleo/archive/. The data used to produce the figures are available here: https://doi.org/10.5281/zenodo.5776909.

References

Arora, V. K., Katavouta, A., Williams, R. G., Jones, C. D., Brovkin, V., Friedlingstein, P., et al. (2020). Carbon–concentration and carbon–climate feedbacks in CMIP6 models and their comparison to CMIP5 models. *Biogeosciences*, *17*, 4173–4222. https://doi.org/10.5194/bg-17-4173-2020

Bé, M.-M., Chisté, V., Dulieu, C., Mougeot, X., Chechev, V. P., Kondev, F. G., et al. (2013). *Table of radionuclides, volume 7 of Monographie BIPM-5*. Bureau International des Poids et Mesures, Pavillon de Breteuil, F-92310 Sèvres.

Acknowledgments

The authors thank the editor and the two reviewers for their helpful comments. The authors thank Tobias Naegler and Ingeborg Levin for providing their ^{14}C production and atmospheric data and Thomas Frölicher, Jens Terhaar, and Sebastian Lienert for comments and the CESM isotope group under the lead of Esther Brady for general support. This work was funded by the Swiss National Science Foundation (#200020_172476 and #200020_200511). All simulations were performed at the Swiss National Supercomputing Centre, CSCS, Lugano, within the projects ISOCARBON and ISOCARBON II. This project has received funding from the European Union's Horizon 2020 research and innovation programme under grant agreement No. 820989 (project COMFORT, Our common future ocean in the Earth system—quantifying coupled cycles of carbon, oxygen, and nutrients for determining and achieving safe operating spaces with respect to tipping points) and under grant agreement No. 821003 (project 4C, Climate-Carbon Interactions in the Current Century). The work reflects only the authors' view; the European Commission and their executive agency are not responsible for any use that may be made of the information the work contains. Open access funding provided by Universitat Bern.

Bolin, B., & Rodhe, H. (1973). A note on the concepts of age distribution and transit time in natural reservoirs. *Tellus*, *25*, 58–62. https://doi.org/10.3402/tellusa.v25i1.9644

Braziunas, T. F., Fung, I. Y., & Stuiver, M. (1995). The preindustrial atmospheric $^{14}CO_2$ latitudinal gradient as related to exchanges among atmospheric, oceanic, and terrestrial reservoirs. *Global Biogeochemical Cycles*, *9*, 565–584. https://doi.org/10.1029/95gb01725

Broecker, W. S., Peng, T.-H., Ostlund, G., & Stuiver, M. (1985). The distribution of bomb radiocarbon in the ocean. *Journal of Geophysical Research*, *90*, 6953–6970. https://doi.org/10.1029/JC090iC04p06953

Danabasoglu, G., Bates, S. C., Briegleb, B. P., Jayne, S. R., Jochum, M., Large, W. G., et al. (2012). The CCSM4 ocean component. *Journal of Climate*, *25*, 1361–1389. https://doi.org/10.1175/JCLI-D-11-00091.1

Danabasoglu, G., Lamarque, J. F., Bacmeister, J., Bailey, D. A., DuVivier, A. K., Edwards, J., et al. (2020). The Community Earth System Model Version 2 (CESM2). *Journal of Advances in Modeling Earth Systems*, *12*, e2019MS001916. https://doi.org/10.1029/2019MS001916

Danabasoglu, G., Peacock, S., Lindsay, K., & Tsumune, D. (2009). Sensitivity of CFC-11 uptake to physical initial conditions and interannually varying surface forcing in a global ocean model. *Ocean Modelling*, *29*, 58–65. https://doi.org/10.1016/j.ocemod.2009.02.011

Dentith, J. E., Ivanovic, R. F., Gregoire, L. J., Tindall, J. C., Robinson, L. F., & Valdes, P. J. (2019). Simulating oceanic radiocarbon with the FAMOUS GCM: Implications for its use as a proxy for ventilation and carbon uptake. *Biogeosciences Discussions*, *2019*, 1–46. https://doi.org/10.5194/bg-2019-365

Dirmeyer, P. A., Gao, X., Zhao, M., Guo, Z., Oki, T., & Hanasaki, N. (2006). GSWP-2: Multimodel analysis and implications for our perception of the land surface. *Bulletin of the American Meteorological Society*, *87*, 1381–1398. https://doi.org/10.1175/BAMS-87-10-1381

Druffel, E. R. M. (2002). Radiocarbon in corals: Records of the carbon cycle, surface circulation and climate. *Oceanography*, *15*, 122–127. https://doi.org/10.5670/oceanog.2002.43

Eide, M., Olsen, A., Ninnemann, U. S., & Johannessen, T. (2017). A global ocean climatology of preindustrial and modern ocean $\delta^{13}C$. *Global Biogeochemical Cycles*, *31*, 515–534. https://doi.org/10.1002/2016gb005473

Enting, I. (1982). *Nuclear weapons data for use in carbon cycle modelling*. CSIRO Division of Marine and Atmospheric Research.

Eyring, V., Bony, S., Meehl, G. A., Senior, C. A., Stevens, B., Stouffer, R. J., & Taylor, K. E. (2016). Overview of the Coupled Model Intercomparison Project Phase 6 (CMIP6) experimental design and organization. *Geoscientific Model Development*, *9*, 1937–1958. https://doi.org/10.5194/gmd-9-1937-2016

Fallon, S. J., & Guilderson, T. P. (2008). Surface water processes in the Indonesian throughflow as documented by a high-resolution coral $\Delta^{14}C$ record. *Journal of Geophysical Research*, *113*. https://doi.org/10.1029/2008JC004722

Friedlingstein, P., Jones, M. W., O'Sullivan, M., Andrew, R. M., Hauck, J., Peters, G. P., et al. (2019). Global carbon budget 2019. *Earth System Science Data*, *11*, 1783–1838. https://doi.org/10.5194/essd-11-1783-2019

Friedlingstein, P., O'Sullivan, M., Jones, M. W., Andrew, R. M., Hauck, J., Olsen, A., et al. (2020). Global carbon budget 2020. *Earth System Science Data*, *12*, 3269–3340. https://doi.org/10.5194/essd-12-3269-2020

Garcia, H. E., Locarnini, R. A., Boyer, T. P., Antonov, J. I., Baranova, O. K., Zweng, M. M., et al. (2013). *World Ocean Atlas 2013. Volume 4: Dissolved inorganic nutrients (phosphate, nitrate, silicate)*. https://doi.org/10.7289/V5J67DWD

Garcia, H. E., Weathers, K., Paver, C. R., Smolyar, I., Boyer, T. P., Locarnini, R. A., et al. (2018). *World Ocean Atlas 2018. Volume 4: Dissolved inorganic nutrients (phosphate, nitrate and nitrate+nitrite, silicate)* (p. 35). https://www.ncei.noaa.gov/access/world-ocean-atlas-2018/

Graven, H., Allison, C. E., Etheridge, D. M., Hammer, S., Keeling, R. F., Levin, I., et al. (2017). Compiled records of carbon isotopes in atmospheric CO_2 for historical simulations in CMIP6. *Geoscientific Model Development*, *10*, 4405–4417. https://doi.org/10.5194/gmd-10-4405-2017

Graven, H. D. (2015). Impact of fossil fuel emissions on atmospheric radiocarbon and various applications of radiocarbon over this century. *Proceedings of the National Academy of Sciences*, *112*, 9542–9545. https://doi.org/10.1073/pnas.1504467112

Graven, H. D., & Gruber, N. (2011). Continental-scale enrichment of atmospheric $^{14}CO_2$ from the nuclear power industry: Potential impact on the estimation of fossil fuel-derived CO_2. *Atmospheric Chemistry and Physics*, *11*, 12339–12349. https://doi.org/10.5194/acp-11-12339-2011

Graven, H. D., Gruber, N., Key, R., Khatiwala, S., & Giraud, X. (2012). Changing controls on oceanic radiocarbon: New insights on shallow-to-deep ocean exchange and anthropogenic CO_2 uptake. *Journal of Geophysical Research*, *117*, C10005. https://doi.org/10.1029/2012jc008074

Griffies, S. M., Danabasoglu, G., Durack, P. J., Adcroft, A. J., Balaji, V., Böning, C. W., et al. (2016). OMIP contribution to CMIP6: Experimental and diagnostic protocol for the physical component of the Ocean Model Intercomparison Project. *Geoscientific Model Development*, *9*, 3231–3296. https://doi.org/10.5194/gmd-9-3231-2016

Grottoli, A. G., & Eakin, C. M. (2007). A review of modern coral $\delta^{18}O$ and $\Delta^{14}C$ proxy records. *Earth-Science Reviews*, *81*, 67–91. https://doi.org/10.1016/j.earscirev.2006.10.001

Grumet, N., Guilderson, T. P., & Dunbar, R. B. (2002). Pre-bomb radiocarbon variability inferred from a Kenyan coral record. *Radiocarbon*, *44*, 581–590. https://doi.org/10.1017/s0033822200031933

Guilderson, T. P., Fallon, S., Moore, M. D., Schrag, D. P., & Charles, C. D. (2009). Seasonally resolved surface water $\Delta^{14}C$ variability in the Lombok Strait: A coralline perspective. *Journal of Geophysical Research*, *114*. https://doi.org/10.1029/2008JC004876

Guilderson, T. P., Schrag, D. P., & Cane, M. A. (2004). Surface water mixing in the Solomon Sea as documented by a high-resolution coral ^{14}C record. *Journal of Climate*, *17*, 1147–1156. https://doi.org/10.1175/1520-0442(2004)017<1147:SWMITS>2.0.CO;2

Guilderson, T. P., Schrag, D. P., Goddard, E., Kashgarian, M., Wellington, G. M., & Linsley, B. K. (2000). Southwest subtropical Pacific surface water radiocarbon in a high-resolution coral record. *Radiocarbon*, *42*, 249–256. https://doi.org/10.1017/S0033822200059051

He, Y., Trumbore, S. E., Torn, M. S., Harden, J. W., Vaughn, L. J. S., Allison, S. D., & Randerson, J. T. (2016). Radiocarbon constraints imply reduced carbon uptake by soils during the 21st century. *Science*, *353*, 1419–1424. https://doi.org/10.1126/science.aad4273

Hesshaimer, V., Heimann, M., & Levin, I. (1994). Radiocarbon evidence for a smaller oceanic carbon dioxide sink than previously believed. *Nature*, *370*, 201–203. https://doi.org/10.1038/370201a0

Hogg, A. G., Heaton, T. J., Hua, Q., Palmer, J. G., Turney, C. S. M., Southon, J., et al. (2020). SHCal20 Southern Hemisphere calibration, 0–55,000 years cal BP. *Radiocarbon*, *62*, 759–778. https://doi.org/10.1017/RDC.2020.59

Hurrell, J. W., Holland, M. M., Gent, P. R., Ghan, S., Kay, J. E., Kushner, P. J., et al. (2013). The Community Earth System Model: A framework for collaborative research. *Bulletin of the American Meteorological Society*, *94*, 1339–1360. https://doi.org/10.1175/bams-d-12-00121.1

Hurtt, G. C., Chini, L., Sahajpal, R., Frolking, S., Bodirsky, B. L., Calvin, K., et al. (2020). Harmonization of global land use change and management for the period 850–2100 (LUH2) for CMIP6. *Geoscientific Model Development*, *13*, 5425–5464. https://doi.org/10.5194/gmd-13-5425-2020

Jahn, A., Lindsay, K., Giraud, X., Gruber, N., Otto-Bliesner, B. L., Liu, Z., & Brady, E. C. (2015). Carbon isotopes in the ocean model of the Community Earth System Model (CESM1). *Geoscientific Model Development*, *8*, 2419–2434. https://doi.org/10.5194/gmd-8-2419-2015

Jones, C. D., Arora, V., Friedlingstein, P., Bopp, L., Brovkin, V., Dunne, J., et al. (2016). C4MIP – The coupled climate–carbon cycle model Intercomparison project: Experimental protocol for CMIP6. *Geoscientific Model Development*, *9*, 2853–2880. https://doi.org/10.5194/gmd-9-2853-2016

Joos, F. (1994). Bomb radiocarbon – Imbalance in the budget. *Nature*, *370*, 181–182. https://doi.org/10.1038/370181a0

Joos, F., & Bruno, M. (1998). Long-term variability of the terrestrial and oceanic carbon sinks and the budgets of the carbon isotopes ^{13}C and ^{14}C. *Global Biogeochemical Cycles*, *12*, 277–295. https://doi.org/10.1029/98gb00746

Joos, F., Meyer, R., Bruno, M., & Leuenberger, M. (1999). The variability in the carbon sinks as reconstructed for the last 1000 years. *Geophysical Research Letters*, *26*, 1437–1440. https://doi.org/10.1029/1999gl900250

Kanu, A. M., Comfort, L. L., Guilderson, T. P., Cameron-Smith, P. J., Bergmann, D. J., Atlas, E. L., et al. (2016). Measurements and modeling of contemporary radiocarbon in the stratosphere. *Geophysical Research Letters*, *43*, 1399–1406. https://doi.org/10.1002/2015gl066921

Keller, K. M., Lienert, S., Bozbiyik, A., Stocker, T. F., Churakova, O. V., Frank, D. C., et al. (2017). 20th century changes in carbon isotopes and water-use efficiency: Tree-ring-based evaluation of the CLM4.5 and LPX-Bern models. *Biogeosciences*, *14*, 2641–2673. https://doi.org/10.5194/bg-14-2641-2017

Kennedy, D., Swenson, S., Oleson, K. W., Lawrence, D. M., Fisher, R., Lola da Costa, A. C., & Gentine, P. (2019). Implementing plant hydraulics in the Community Land Model, version 5. *Journal of Advances in Modeling Earth Systems*, *11*, 485–513. https://doi.org/10.1029/2018MS001500

Key, R. M., Kozyr, A., Sabine, C. L., Lee, K., Wanninkhof, R., Bullister, J. L., et al. (2004). A global ocean carbon climatology: Results from global data analysis project (GLODAP). *Global Biogeochemical Cycles*, *18*, GB4031. https://doi.org/10.1029/2004GB002247

Khatiwala, S., Primeau, F., & Holzer, M. (2012). Ventilation of the deep ocean constrained with tracer observations and implications for radiocarbon estimates of ideal mean age. *Earth and Planetary Science Letters*, *325–326*, 116–125. https://doi.org/10.1016/j.epsl.2012.01.038

Kilbourne, K. H., Quinn, T. M., Guilderson, T. P., Webb, R. S., & Taylor, F. W. (2007). Decadal- to interannual-scale source water variations in the Caribbean Sea recorded by Puerto Rican coral radiocarbon. *Climate Dynamics*, *29*, 51–62. https://doi.org/10.1007/s00382-007-0224-2

Kobayashi, S., Ota, Y., Harada, Y., Ebita, A., Moriya, M., Onoda, H., et al. (2015). The JRA-55 reanalysis: General specifications and basic characteristics. *Journal of the Meteorological Society of Japan. Ser. II*, *93*, 5–48. https://doi.org/10.2151/jmsj.2015-001

Kovaltsov, G. A., Mishev, A., & Usoskin, I. G. (2012). A new model of cosmogenic production of radiocarbon ^{14}C in the atmosphere. *Earth and Planetary Science Letters*, *337–338*, 114–120. https://doi.org/10.1016/j.epsl.2012.05.036

Koven, C. D., Riley, W. J., Subin, Z. M., Tang, J. Y., Torn, M. S., Collins, W. D., et al. (2013). The effect of vertically resolved soil biogeochemistry and alternate soil C and N models on C dynamics of CLM4. *Biogeosciences*, *10*, 7109–7131. https://doi.org/10.5194/bg-10-7109-2013

Krakauer, N. Y., Randerson, J. T., Primeau, F. W., Gruber, N., & Menemenlis, D. (2006). Carbon isotope evidence for the latitudinal distribution and wind speed dependence of the air-sea gas transfer velocity. *Tellus, Serie B*, *58B*, 390–417. https://doi.org/10.1111/j.1600-0889.2006.00223.x

Large, W. G., & Yeager, S. G. (2009). The global climatology of an interannually varying air–sea flux data set. *Climate Dynamics*, *33*, 341–364. https://doi.org/10.1007/s00382-008-0441-3

Lawrence, C. R., Beem-Miller, J., Hoyt, A. M., Monroe, G., Sierra, C. A., Stoner, S., et al. (2020). An open-source database for the synthesis of soil radiocarbon data: International Soil Radiocarbon Database (ISRaD) version 1.0. *Earth System Science Data*, *12*, 61–76. https://doi.org/10.5194/essd-12-61-2020

Lawrence, D. M., Fisher, R. A., Koven, C. D., Oleson, K. W., Swenson, S. C., Bonan, G., et al. (2019). The Community Land Model version 5: Description of new features, Benchmarking, and impact of forcing uncertainty. *Journal of Advances in Modeling Earth Systems*, *11*, 4245–4287. https://doi.org/10.1029/2018MS001583

Laws, E. A., Popp, B. N., Bidigare, R. R., Kennicutt, M. C., & Macko, S. A. (1995). Dependence of phytoplankton carbon isotopic composition on growth rate and $[CO_2)_{aq}$: Theoretical considerations and experimental results. *Geochimica et Cosmochimica Acta*, *59*, 1131–1138. https://doi.org/10.1016/0016-7037(95)00030-4

Levin, I., Naegler, T., Kromer, B., Diehl, M., Francey, R. J., Gomez-Pelaez, A. J., et al. (2010). Observations and modelling of the global distribution and long-term trend of atmospheric $^{14}CO_2$. *Tellus B: Chemical and Physical Meteorology*, *62*, 26–46. https://doi.org/10.1111/j.1600-0889.2009.00446.x

Lombardozzi, D. L., Lu, Y., Lawrence, P. J., Lawrence, D. M., Swenson, S., Oleson, K. W., et al. (2020). Simulating agriculture in the Community Land Model version 5. *Journal of Geophysical Research: Biogeosciences*, *125*, e2019JG005529. https://doi.org/10.1029/2019JG005529

Masarik, J., & Beer, J. (2009). An updated simulation of particle fluxes and cosmogenic nuclide production in the Earth's atmosphere. *Journal of Geophysical Research*, *114*, D11103. https://doi.org/10.1029/2008jd010557

Matsumoto, K., Sarmiento, J. L., Key, R. M., Aumont, O., Bullister, J. L., Caldeira, K., et al. (2004). Evaluation of ocean carbon cycle models with data-based metrics. *Geophysical Research Letters*, *31*. https://doi.org/10.1029/2003gl018970

Meinshausen, M., Vogel, E., Nauels, A., Lorbacher, K., Meinshausen, N., Etheridge, D. M., et al. (2017). Historical greenhouse gas concentrations for climate modelling (CMIP6). *Geoscientific Model Development*, *10*, 2057–2116. https://doi.org/10.5194/gmd-10-2057-2017

Moore, J. K., Doney, S. C., Kleypas, J. A., Glover, D. M., & Fung, I. Y. (2002). An intermediate complexity marine ecosystem model for the global domain. *Deep Sea Research Part II: Topical Studies in Oceanography*, *49*, 403–462. https://doi.org/10.1016/S0967-0645(01)00108-4

Moore, J. K., Doney, S. C., & Lindsay, K. (2004). Upper ocean ecosystem dynamics and iron cycling in a global three-dimensional model. *Global Biogeochemical Cycles*, *18*. https://doi.org/10.1029/2004GB002220

Mouchet, A. (2013). The ocean bomb radiocarbon inventory revisited. *Radiocarbon*, *55*, 1580–1594. https://doi.org/10.1017/S0033822200048505

Müller, S. A., Joos, F., Plattner, G. K., Edwards, N. R., & Stocker, T. F. (2008). Modeled natural and excess radiocarbon: Sensitivities to the gas exchange formulation and ocean transport strength. *Global Biogeochemical Cycles*, *22*, GB3011. https://doi.org/10.1029/2007GB003065

Naegler, T. (2009). Reconciliation of excess ^{14}C-constrained global CO_2 piston velocity estimates. *Tellus B: Chemical and Physical Meteorology*, *61*, 372–384. https://doi.org/10.1111/j.1600-0889.2008.00408.x

Naegler, T., & Levin, I. (2006). Closing the global radiocarbon budget 1945–2005. *Journal of Geophysical Research*, *111*. https://doi.org/10.1029/2005jd006758

Naegler, T., & Levin, I. (2009a). Observation-based global biospheric excess radiocarbon inventory 1963–2005. *Journal of Geophysical Research*, *114*. https://doi.org/10.1029/2008jd011100

Naegler, T., & Levin, I. (2009b). Biosphere-atmosphere gross carbon exchange flux and the $\delta^{13}CO_2$ and $\Delta^{14}CO_2$ disequilibria constrained by the biospheric excess radiocarbon inventory. *Journal of Geophysical Research*, *114*. https://doi.org/10.1029/2008JD011116

Oeschger, H., Siegenthaler, U., Schotterer, U., & Gugelmann, A. (1975). A box diffusion model to study the carbon dioxide exchange in nature. *Tellus*, *27*, 170–192. https://doi.org/10.3402/tellusa.v27i2.9900

Oleson, K., Lawrence, D. M., Bonan, G. B., Drewniak, B., Huang, M., Koven, C. D., et al. (2013). *Technical description of version 4.5 of the Community Land Model (CLM)* (p. 420). National Centre for Atmospheric Research (No. NCAR/TN-503+STR). https://doi.org/10.5065/D6RR1W7M

Orr, J. C., Najjar, R. G., Aumont, O., Bopp, L., Bullister, J. L., Danabasoglu, G., et al. (2017). Biogeochemical protocols and diagnostics for the CMIP6 Ocean Model Intercomparison Project (OMIP). *Geoscientific Model Development*, *10*, 2169–2199. https://doi.org/10.5194/gmd-10-2169-2017

Orr, J. C., Najjar, R. G., Sabine, C., & Joos, F. (1999). *OCMIP-2 Abiotic-HOWTO*. Retrieved from http://ocmip5.ipsl.jussieu.fr/OCMIP/phase2/simulations/Abiotic/HOWTO-Abiotic.html

Peacock, S. (2004). Debate over the ocean bomb radiocarbon sink: Closing the gap. *Global Biogeochemical Cycles*, *18*. https://doi.org/10.1029/2003GB002211

Randerson, J. T., Enting, I. G., Schuur, E. A. G., Caldeira, K., & Fung, I. Y. (2002). Seasonal and latitudinal variability of troposphere $\Delta^{14}CO_2$: Post bomb contributions from fossil fuels, oceans, the stratosphere, and the terrestrial biosphere. *Global Biogeochemical Cycles*, *16*, 59–1–59–19. https://doi.org/10.1029/2002GB001876

Rath, H. (1988). *Simulation der globalen ^{85}Kr- und $^{14}CO_2$-Verteilung mit Hilfe eines zeitabhängigen, zweidimensionalen Modells der Atmosphäre* (Ph.D. Dissertation). Universität Heidelberg.

Reimer, P. J., Austin, W. E. N., Bard, E., Bayliss, A., Blackwell, P. G., Bronk Ramsey, C., et al. (2020). The IntCal20 Northern hemisphere radiocarbon age calibration curve (0–55 cal kBP). *Radiocarbon*, *62*, 725–757. https://doi.org/10.1017/RDC.2020.41

Revelle, R., & Suess, H. E. (1957). Carbon dioxide exchange between atmosphere and ocean and the question of an increase of atmospheric CO_2 during the past decades. *Tellus*, *9*, 18–27. https://doi.org/10.3402/tellusa.v9i1.9075

Rodgers, K. B., Aumont, O., Madec, G., Menkes, C., Blanke, B., Monfray, P., et al. (2004). Radiocarbon as a thermocline proxy for the eastern equatorial Pacific. *Geophysical Research Letters*, *31*. https://doi.org/10.1029/2004GL019764

Rodgers, K. B., Mikaloff-Fletcher, S. E., Bianchi, D., Beaulieu, C., Galbraith, E. D., Gnanadesikan, A., et al. (2011). Interhemispheric gradient of atmospheric radiocarbon reveals natural variability of Southern Ocean winds. *Climate of the Past*, *7*, 1123–1138. https://doi.org/10.5194/cp-7-1123-2011

Roth, R., & Joos, F. (2013). A reconstruction of radiocarbon production and total solar irradiance from the holocene ^{14}C and CO_2 records: Implications of data and model uncertainties. *Climate of the Past*, *9*, 1879–1909. https://doi.org/10.5194/cp-9-1879-2013

Schmidt, A., Burr, G. S., Taylor, F. W., O'Malley, J., & Beck, J. W. (2004). A semiannual radiocarbon record of a modern coral from the Solomon Islands. *Nuclear Instruments and Methods in Physics Research Section B: Beam Interactions with Materials and Atoms*, *223–224*, 420–427. https://doi.org/10.1016/j.nimb.2004.04.080

Shi, Z., Allison, S. D., He, Y., Levine, P. A., Hoyt, A. M., Beem-Miller, J., et al. (2020). The age distribution of global soil carbon inferred from radiocarbon measurements. *Nature Geoscience*, *13*, 555–559. https://doi.org/10.1038/s41561-020-0596-z

Siegenthaler, U. (1989). Carbon-14 in the oceans. In P. Fritz & J. C.Fontes (Eds.), *Handbook of environmental isotope geochemistry*. Elsevier.

Siegenthaler, U., & Joos, F. (1992). Use of a simple-model for studying oceanic tracer distributions and the global carbon-cycle. *Tellus Series B: Chemical and Physical Meteorology*, *44*, 186–207. https://doi.org/10.3402/tellusb.v44i3.15441

Suess, H. E. (1955). Radiocarbon concentration in modern wood. *Science*, *122*, 415–417. https://www.science.org/doi/10.1126/science.122.3166.415.b

Sweeney, C., Gloor, E., Jacobson, A. R., Key, R. M., McKinley, G., Sarmiento, J. L., & Wanninkhof, R. (2007). Constraining global air-sea gas exchange for CO_2 with recent bomb ^{14}C measurements. *Global Biogeochemical Cycles*, *21*. https://doi.org/10.1029/2006GB002784

Talley, L. D. (2013). Closure of the global overturning circulation through the Indian, Pacific, and Southern Oceans: Schematics and transports. *Oceanography*, *26*, 80–97. https://doi.org/10.5670/oceanog.2013.07

Terhaar, J., Frölicher, T. L., & Joos, F. (2021). Southern Ocean anthropogenic carbon sink constrained by sea surface salinity. *Science Advances*, *7*, eabd5964. https://doi.org/10.1126/sciadv.abd5964

Thompson, M. V., Randerson, J. T., Malmström, C. M., & Field, C. B. (1996). Change in net primary production and heterotrophic respiration: How much is necessary to sustain the terrestrial carbon sink? *Global Biogeochemical Cycles*, *10*, 711–726. https://doi.org/10.1029/96gb01667

Toggweiler, J. R., Dixon, K., & Bryan, K. (1989). Simulations of radiocarbon in a coarse-resolution world ocean model: 1. Steady state prebomb distributions. *Journal of Geophysical Research*, *94*, 8217–8242. https://doi.org/10.1029/JC094iC06p08217

Turnbull, J. C., Mikaloff Fletcher, S. E., Ansell, I., Brailsford, G. W., Moss, R. C., Norris, M. W., & Steinkamp, K. (2017). Sixty years of radiocarbon dioxide measurements at Wellington, New Zealand: 1954–2014. *Atmospheric Chemistry and Physics*, *17*, 14771–14784. https://doi.org/10.5194/acp-17-14771-2017

Wanninkhof, R. (2014). Relationship between wind speed and gas exchange over the ocean revisited. *Limnology and Oceanography: Methods*, *12*, 351–362. https://doi.org/10.4319/lom.2014.12.351

Yang, X., North, R., & Romney, C. (2000). *CMR nuclear explosion database (revision 3)*. Center for Monitoring Research, U. S. Army Space and Missile Defense Command.

Zazzeri, G., Acuña Yeomans, E., & Graven, H. D. (2018). Global and regional emissions of radiocarbon from nuclear power plants from 1972 to 2016. *Radiocarbon*, *60*, 1067–1081. https://doi.org/10.1017/RDC.2018.42

Zhang, J., Quay, P. D., & Wilbur, D. O. (1995). Carbon isotope fractionation during gas-water exchange and dissolution of CO_2. *Geochimica et Cosmochimica Acta*, *59*, 107–114. https://doi.org/10.1016/0016-7037(95)91550-D